Nanoscale Horizons

ROYAL SOCIETY OF CHEMISTRY

REVIEW

View Article Online
View Journal

Cite this: DOI: 10.1039/d6nh00001k

From plant transpiration to hydrovoltaics: distributed energy harvesting driven by water evaporation

Jongbin Won[a] and Albert Tianxiang Liu *[abcd]

Evaporation continuously converts absorbed solar heat into the kinetic motion of water molecules, creating a ubiquitous driving force that remains largely untapped for direct electricity generation. In plants, this process is harnessed through transpiration, where capillary flow and sustained negative pressure drive long-range water transport without moving parts. Inspired by this natural hydraulic engine, transpiration-inspired hydrovoltaics (TIH) have emerged as solid-state material platforms that convert evaporation-driven water transport into electrical output through interfacial electrokinetic processes. In this review, we introduce a unified physical framework for TIH by explicitly connecting the physics of plant transpiration to evaporation-driven electricity harvesting in engineered porous media. We summarize the governing principles of water ascent in trees, including capillarity, water-potential gradients and cohesion–tension stability, and map these concepts onto synthetic TIH architectures built from hydrophilic micro- and nanofluidic networks. We critically examine the proposed electricity-generation mechanisms in TIH, including classical streaming potentials on insulating substrates, pseudo-streaming in conductive porous networks and ionovoltaic coupling in semiconducting channels. We systematically elucidate how geometry, pore microarchitecture, surface chemistry, electrical conductivity and environmental conditions such as humidity, temperature and airflow jointly govern device performance. By benchmarking TIH against decades of quantitative insight from plant hydraulics, we identify key trade-offs, unresolved mechanistic questions, and actionable design opportunities for robust, scalable evaporation-driven power generation and self-powered sensing. Together, these perspectives position TIH as a promising platform for distributed energy harvesting at the water–energy nexus.

Received 2nd January 2026,
Accepted 8th April 2026

DOI: 10.1039/d6nh00001k

rsc.li/nanoscale-horizons

1. Introduction

Nearly all renewable energy originates from the sun, with the Earth's atmosphere, oceans, and landmasses absorbing approximately 3 850 000 exajoules annually. Water absorbs and redistributes a large fraction of incoming solar energy, translating to an estimated 60 petawatts per year,[1] three orders of magnitude greater than the annual global energy consumption. Most of this absorbed energy dissipates as thermal and vibrational energy (molecular motion), driving water evaporation, a spontaneous and continuous phase transition from liquid to vapor that sustains the Earth's water cycle.[1–3] It should be noted that water itself contains little intrinsically harvestable chemical energy in its molecular bonds. Instead, the only exploitable energy associated with water comes from the physical (thermal and mechanical) energy it carries. Water serves as the carrier, not the source, of energy that can be harvested.[4]

The kinetic energy of water has been exploited for centuries, with early civilizations using water wheels and mills to convert bulk water flow into mechanical power.[5] Today, hydroelectric power that converts the kinetic energy of collected bulk water flow into electricity using turbines is a major source of renewable electricity. This progression reflects a recurring theme: water's energy has been easiest to harvest when it is organized into large-scale, directed motion. Yet the water cycle begins in almost a completely opposite fashion, namely through highly distributed, molecular-scale evaporation processes occurring across open waters, soils, and vegetation. Consequently, even though a modern turbine can easily convert bulk kinetic energy into electricity with over 90% efficiency,[6] less than 0.003% of evaporated water is ever collected inside a reservoir

[a] Department of Chemical Engineering, University of Michigan, Ann Arbor, MI, 48109, USA. E-mail: atliu@umich.edu; Tel: +1-734-763-5192
[b] Department of Material Science and Engineering, University of Michigan, Ann Arbor, MI 48109, USA
[c] Macromolecular Science and Engineering, University of Michigan, Ann Arbor, Michigan 48109, USA
[d] Biointerfaces Institute, University of Michigan, Ann Arbor, MI, USA

and stored behind a dam.[7] As a result, the vast thermal energy driving the evaporation process every day still remains largely untapped.

This contrast motivates a simple question: why capture water's energy primarily at the end of the water cycle, after vapor condenses, precipitation occurs, and flow concentrates into rivers, rather than closer to the source of evaporation? From a physics standpoint, evaporation is where thermal input is first converted into nonequilibrium molecular transport. If that dispersed transport could be rectified into electrical output locally, the water cycle would offer an additional, spatially distributed route for energy conversion that complements conventional hydroelectric power.

The primary obstacle in harvesting evaporative energy lies in its molecular scale nature. Conventional kinetic-to-electric conversion tools, such as turbines, require concentrated flow and well-defined momentum transfer to operate efficiently. Evaporation-driven transport, by contrast, occurs at the scale of individual water molecules, making it difficult to capture using conventional means.[8] A molecular-scale problem calls for a molecular-scale solution. To harness the kinetic energy of evaporating water molecules, we need to develop nanoscale energy converters, even if they look nothing like their macroscopic counterparts. We need nanoscale architectures that efficiently couple molecular motion to electronic charge transport. This requirement helps explain why direct evaporative energy capture has long remained more of a conceptual opportunity than a widely realized technology.

Recent advances in nanomaterials and porous functional media have begun to close this gap.[9,10] The key advantage of nanomaterials lies in their high surface-area-to-volume ratios, which facilitate molecular-scale interactions necessary for capturing water's kinetic energy. Additionally, nanomaterials exhibit quantum confinement effects[11] and strong surface phonon–electron coupling,[12] enhancing direct mechanical-to-electrical energy conversion efficiency from adsorbed molecules. Indeed, these nanostructured solid-state materials have been demonstrated to sustain capillary-driven flow, maintain evaporation at exposed interfaces,[13] and mediate interfacial charge separation *via* surface functional groups and electric double layers (EDLs).[14,15] This electrokinetic phenomenon, known as the hydrovoltaic (HV) effect, provides a direct means of capturing molecular scale water motion into useable electricity.

Nature provides a compelling proof-of-principle that evaporation can sustain persistent transport and do useful work. Through transpiration, plants continuously pump water and nutrients over long distances, often tens of meters, without moving parts. Distributed evaporation at leaves generates and maintains negative pressures in the xylem, while hierarchical porous transport networks and the cohesion–tension stability of water sustain flow under ambient conditions. Importantly for hydrovoltaics, the same features that enable transpiration, including confined water pathways, structured interfaces, and sustained pressure gradients, also create conditions under which interfacial ion transport and charge separation can be amplified and controlled.

Jongbin Won

Mr Jongbin Won is a PhD candidate in Laboratory of Emergent and Galvanically Orchestrated Systems (LEGOS) in the department of Chemical Engineering at the University of Michigan. He received his BS degree from Seoul National University of Science and Technology (Seoul Tech), and MS degree from Seoul National University (SNU). His current research focuses on energy harvesting via hydrovoltaics based on physicochemical theory and experimental applications through material synthesis and device fabrication.

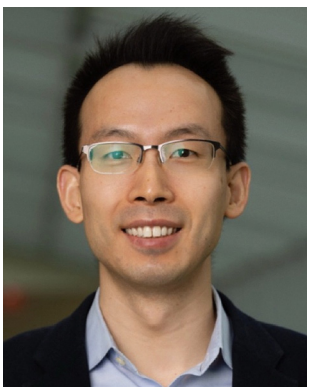

Albert Tianxiang Liu

Prof. Albert Tianxiang Liu is an Assistant Professor of Chemical Engineering, Materials Science and Engineering, and Macromolecular Science and Engineering at the University of Michigan, Ann Arbor. He is a member of the Biointerfaces Institute and the Rogel Cancer Center. Albert received his BS in Chemical Engineering from Caltech in 2014 and his PhD in Chemical Engineering from MIT in 2020, working with Prof. Michael Strano. Before joining Michigan, he completed postdoctoral training in the Stanford University School of Medicine with Prof. Steven Chu in 2022. His research group, the Laboratory of Emergent and Galvanically Orchestrated Systems, focuses on colloidal and surface engineering to control nanoscale interfacial transport processes in micro-confined materials. From Prof. Liu: Nanoscale Horizons has become a leading venue for showcasing creative, forward-looking research at the frontiers of nanoscience. We are honored to contribute to this 10th Anniversary collection and grateful for the opportunity to support and celebrate the journal through this work.

Motivated by this connection, we use the term transpiration-inspired hydrovoltaics (TIH) to describe HV systems in which evaporation-driven capillary flow through hydrophilic porous, microfluidic, or nanofluidic networks is central to sustained operation. In HIV devices, porous networks wick water from a reservoir, evaporation drives flow, and interfacial electrokinetic processes convert that flow into electrical output. In this review, we connect transpiration physics to evaporation-driven electricity generation in TIH devices. We first summarize the physical basis of water ascent in trees, then map those principles onto synthetic porous architectures. We examine macroscopic, microscopic, and environmental variables that govern output, discuss the role of electrical conductivity and interfacial chemistry, survey emerging applications, and conclude with key challenges and opportunities for advancing TIH.

2. Transpiration mechanism of trees

Trees regulate water transport by integrating roots, xylem, and stomata into a coupled hydraulic network.[16] Water and dissolved nutrients are taken up from soil, conveyed upward through a hierarchical conduit system, and ultimately released to the atmosphere as vapor through evaporation at the leaves. This sustained ascent of water molecules is remarkable because it occurs without mechanical pumps and routinely overcomes substantial gravitational head. In this section, we summarize the physical basis of transpiration, with emphasis on capillarity, water-potential gradients, and the cohesion–tension framework that rationalizes negative pressure (tension) in xylem water. These concepts provide a foundation for later sections, where evaporation-driven flow in engineered porous networks is coupled to interfacial charge transport in TIH systems (Fig. 1).

2.1 Mechanism of capillary rise and its limitation

Capillary action is a widely recognized driver of water rise in narrow channels. When water contacts a hydrophilic pore or tube, wetting and surface tension form a curved meniscus at the liquid–air interface. The resulting curvature produces a pressure difference across the meniscus that, for an idealized cylindrical capillary, can be approximated by the Young–Laplace relation:

$$\Delta P = \frac{2\gamma\cos\theta}{a} \quad (1)$$

where ΔP is the pressure difference between the liquid and gas phases, γ is the surface tension of water, θ is the contact angle between water and the tube wall, and a is the capillary radius. Capillary rise proceeds until this capillary pressure balances the hydrostatic pressure associated with a liquid column of height h:

$$\rho g h = \frac{2\gamma\cos\theta}{a} \quad (2)$$

where ρ is the density of water and g is the gravitational acceleration. Combining eqn (1) and (2) yields the maximum capillary rise height:

$$h_{\max} = \frac{2\gamma\cos\theta}{a\rho g} \quad (3)$$

This scaling is useful for back-of-the-envelope estimates. Assuming perfect wettability (θ = 0), a tube radius of 10 μm, and using the surface tension and density of water at 25 °C, the maximum capillary rise is estimated to be $h_{\max} \approx 1.5$ m. This is far below the height of many trees and orders of magnitude below the tallest species that exceed 100 m. At the same time, eqn (3) implies that capillary rise can become extremely large as the characteristic pore radius shrinks. For example, if the tube diameter decreases to 10 nm, the same estimate gives $h_{\max} \approx 1500$ m, illustrating that Young–Laplace pressures can be extremely large under nanoscale confinement.

However, predicted heights from eqn (3) do not automatically translate into stable, continuous water columns at those heights. In ordinary conduits under atmospheric pressure, even when an external pump pulls water upward, water columns substantially above about 10 m are difficult to sustain because the liquid enters a tensile state ($\Delta P > 1$ atm in magnitude) and cavitation can nucleate.[23,24] Once gas nuclei or vapour bubbles form, the water column breaks and the tensile state collapses. The discrepancy between simple capillary-rise estimates and the water ascent observed in trees indicates that additional physics beyond static capillarity is required, specifically the generation and maintenance of negative pressure (tension) in a continuous liquid column while suppressing cavitation.[17]

2.2 Driving force of water ascent

In plant physiology, water movement is commonly described in terms of water potential (Ψ), which represents the chemical potential energy of water per unit mass. When expressed in pressure units by incorporating the density of water, Ψ can be interpreted as an effective pressure. Water flows from regions of higher to lower potential. The total water potential is often decomposed into four primary components:

$$\Psi = \psi_{\text{osmosis}} + \psi_{\text{gravity}} + \psi_{\text{matrix}} + \psi_{\text{pressure}} \quad (4)$$

where ψ_{osmosis} is the osmotic potential arising from solute concentration differences across semipermeable membranes, ψ_{gravity} is the gravitational potential reflecting the influence of gravity on water flow, ψ_{matrix} is the matrix potential associated with interactions between water and solid surfaces, and ψ_{pressure} is the pressure potential associated with hydrostatic pressure within the hydraulic pathway.[25] Capillary pressure, introduced in subsection (a), can be incorporated into ψ_{matrix} through the local curvature of liquid–air interfaces within pores.

In plants, a sustained water potential gradient is established along the soil–plant–atmosphere continuum. A common qualitative ordering is:

$$\Psi_{\text{soil}} > \Psi_{\text{root}} > \Psi_{\text{xylem}} > \Psi_{\text{leaf}} > \Psi_{\text{air}} \quad (5)$$

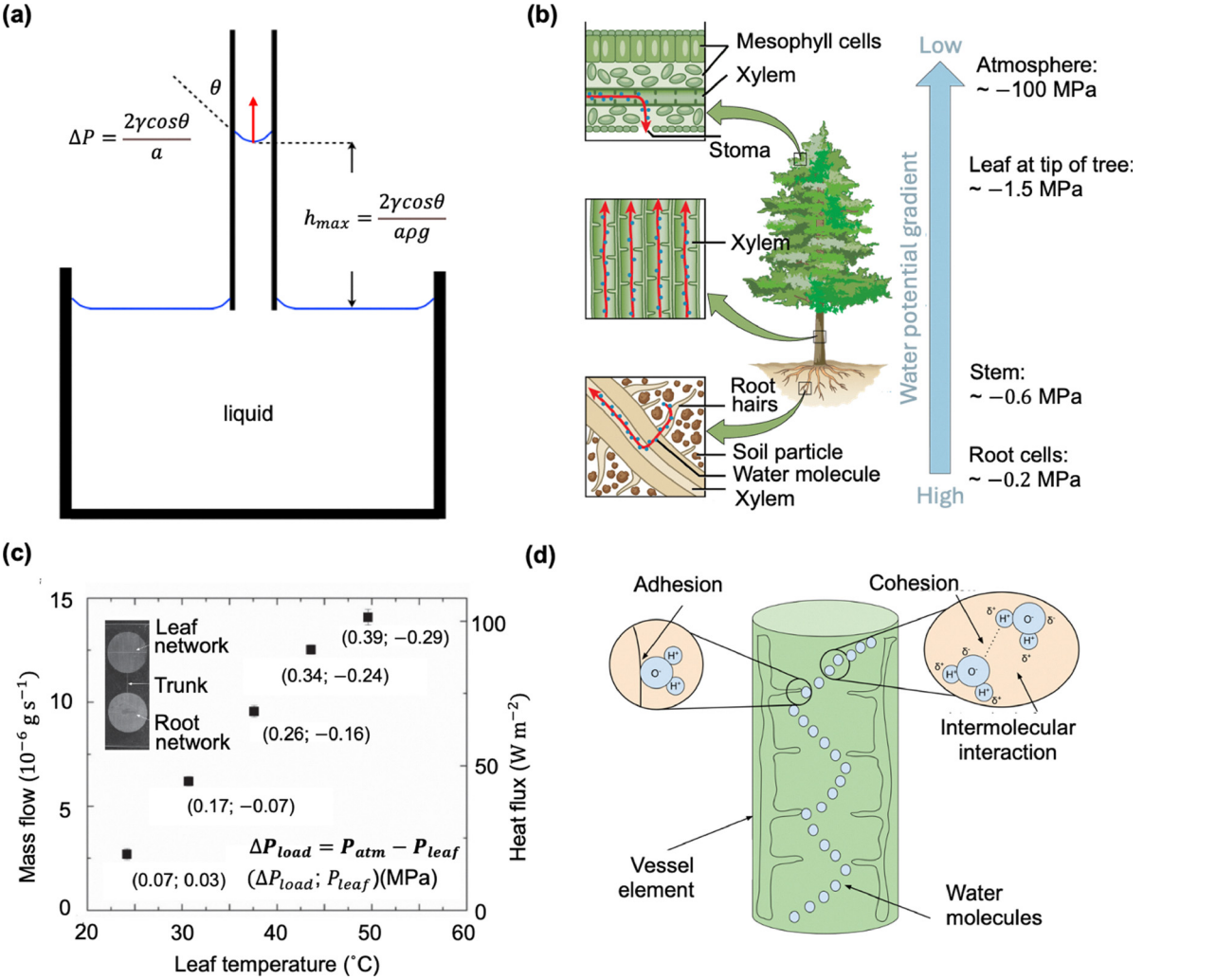

Fig. 1 Water ascent in tree driven by negative pressure, as evidenced experimentally and rationalized by the cohesion–tension theory. (a) Capillary rise in a tube connected to a bulk liquid reservoir. The Young–Laplace relation gives the capillary pressure that drives ascent, and the corresponding expression on the right gives the maximum rise height against gravity. Reproduced with permission.[17] Copyright 2025, Elsevier. (b) Schematic illustration of transpiration through root, xylem, and stoma driven by the water potential gradient. Reproduced with permission.[18] Copyright 2023, Academic Senate for California Community Colleges OER Initiative (ASCCC OERI). (c) Direct measurement of negative pressure in a hydrogel-based synthetic tree. Inset: Photograph of the device comprising a root network, trunk, and leaf network. Reproduced with permission.[19] Copyright 2008, Springer Nature. (d) Cohesion–tension mechanism. Water molecules (blue circles) maintain a continuous liquid column through adhesion to the vessel walls and cohesion between neighboring molecules. Reproduced with permission.[18] Copyright 2023, Academic Senate for California Community Colleges OER Initiative (ASCCC OERI).

where each subscript represents the total water potential in the soil, root, xylem, leaf, and air, respectively.[19] Evaporation at the leaf surface lowers the local water potential by withdrawing water from confined interfacial regions. This maintains a driving force as long as water supply and evaporative demand persist, sustaining continuous flow from soil uptake through root membranes to evaporation through stomata. Remarkably, in many plants, the absolute water potential within the xylem and leaves can reach strongly negative values while water remains liquid. Reported leaf water potentials can approach several negative megapascals relative to soil, despite atmospheric pressure being approximately 0.1 MPa.[27,28] These observations reinforce that the plant hydraulic system does not operate near atmospheric pressure. Instead, it operates under tension.

2.3 Absolute negative pressure confirmed in synthetic tree systems

Negative pressure states have been demonstrated not only in living trees[29–31] but also in synthetic systems that mimic transpiration-driven transport under controlled geometry and boundary conditions.[19,32] A widely cited example is the synthetic tree developed by Wheeler and Stroock.[19] In that study, a hydrogel-based, unidirectional microchannel network was fabricated in poly(2-hydroxyethyl methacrylate) (pHEMA) using soft lithography. The structure consisted of two bundles of straight microchannels representing the root and leaf networks, interconnected by a single microchannel of approximately 10 μm in diameter that served as the trunk. Water was supplied to the root network, transported through the trunk,

and delivered to the leaf network. The root and trunk regions were sealed, whereas the leaf network was exposed to air, thereby localizing evaporation to the leaf-side interface.

The volumetric flow rate from the root to the leaf network was measured, and the corresponding pressure drop was inferred using Poiseuille's law for laminar flow through a cylindrical channel:

$$\Delta p = \frac{8\mu L Q}{\pi R^4} \tag{6}$$

where Δp is the pressure difference between the root and leaf networks, μ is the dynamic viscosity of water, L is the channel length from the root inlet to the leaf region, Q is the volumetric flow rate, and R is the channel radius. Using measured Q and the known trunk geometry, the calculated pressure at the leaf network was approximately 1 MPa lower than that at the root network, corresponding to an absolute negative pressure in the liquid. The boundary condition is clear: evaporation at the exposed leaf network generates a pressure drop that is transmitted through a connected hydraulic pathway. Consistent with this interpretation, simulations predict that pressures below −1 MPa can arise when water flows through micron-scale channels and evaporates into air.[33] Together, these results support the physical plausibility of MPa-scale tension in confined liquid pathways sustained by evaporation.

2.4 Cohesion–tension theory explains the negative pressure in water during transpiration

It is counterintuitive that water can remain liquid under absolute negative pressure, since water typically vaporizes under low-pressure conditions. The cohesion–tension (C–T) theory resolves this by proposing that water in xylem conduits forms a continuous column stabilized by cohesive hydrogen bonding between molecules and adhesive interactions with conduit walls.[34] At the leaf surface, evaporation through stomata withdraws water from confined interfacial regions and lowers the local water potential. This creates a tensile force that pulls on the continuous water column. Because cohesion maintains molecular connectivity, this tension propagates downward through the xylem, drawing water upward from the roots.

A defining feature of the C–T framework is that xylem water exists in a metastable tensile state.[35] This metastability enables water to remain liquid even when the pressure drops below atmospheric pressure and, in some cases, below zero on an absolute pressure scale. As a result, water can be transported to heights far exceeding the capillary-rise scale suggested by eqn (3). At the same time, the tensile state is not unbounded. If the pressure becomes sufficiently negative, water can cavitate, and bubbles can form within xylem conduits, leading to embolisms that reduce hydraulic conductivity.[19,36,37] Cavitation is therefore widely viewed as a key constraint on water ascent and on the operating envelope of transpiration under high evaporative demand.

Several studies have attempted to relate evaporation-associated mass flux to interfacial liquid pressure using kinetic expressions for phase change. One form that has been used is:

$$\dot{m}_e = \frac{2\sigma}{2 - p_v}\sqrt{\frac{M}{2\pi R}}\left(\frac{p_l}{\sqrt{T_l}} - \frac{P_v}{\sqrt{T_v}}\right) \tag{7}$$

where $\dot{m}_e$ is the evaporation mass flux, σ is the accommodation coefficient, M is the molar mass of the fluid, R is the ideal gas constant, p_l is the liquid pressure at the liquid–air interface, P_v is the saturated vapor pressure, and T_l and T_v are the liquid temperature and saturated vapor temperature, respectively.[38] With a sign convention in which $\dot{m}_e$ is defined as the outgoing flux from water to air, $\dot{m}_e$ is negative during evaporation. When other variables are approximately constant, this expression indicates that p_l is coupled to $\dot{m}_e$, linking the evaporative flux at the vapor–liquid interface to the local liquid pressure. In this way, evaporation continuously regenerates the negative pressure needed to sustain upward transport, thereby closing the transpiration cycle.

3. Transpiration-inspired hydrovoltaics: a new energy harvesting paradigm

For a long time, harnessing the water cycle through transpiration was exclusive to plants. Recent advances in nanomaterials and microfabrication have enabled synthetic, tree-like systems built from hydrophilic micro- and nanoporous structures that reproduce the key functional elements of transpiration: capillary forces draw water through confined channels, while evaporation at an exposed surface sustains continuous flow, consistent with the cohesion–tension framework. Building on this analogy, transpiration-driven water transport has been repurposed not only for fluid delivery but also for electricity generation. By maintaining a water-potential gradient along the channel and connecting electrodes at the "root" (bottom) and "leaf" (top) regions, a potential difference can develop across the device and drive current through an external circuit (Fig. 2).

3.1 Advent of transpiration-inspired hydrovoltaics and the operating principle

This concept is realized in hydrovoltaics (HV), an emerging class of technologies that generate electricity from interactions between water (or aqueous electrolytes) and solid substrates.[5,14,39,40] Transpiration-inspired architectures are particularly compelling because they can sustain continuous, relatively stable output under ambient conditions. To mimic plant water transport, TIH devices are constructed from hydrophilic networks with micro- and nanoscale confinement, including natural wood templates, engineered porous membranes, and assemblies of organic or inorganic micro- and nanoparticles. These networks are implemented as thin films on substrates or as free-standing porous matrices. In a canonical configuration, one end of the film or matrix is immersed in a water reservoir so that capillarity wicks liquid into the pore network, while evaporation from exposed surfaces maintains flow. Under these conditions, a voltage and current can develop between the immersed region

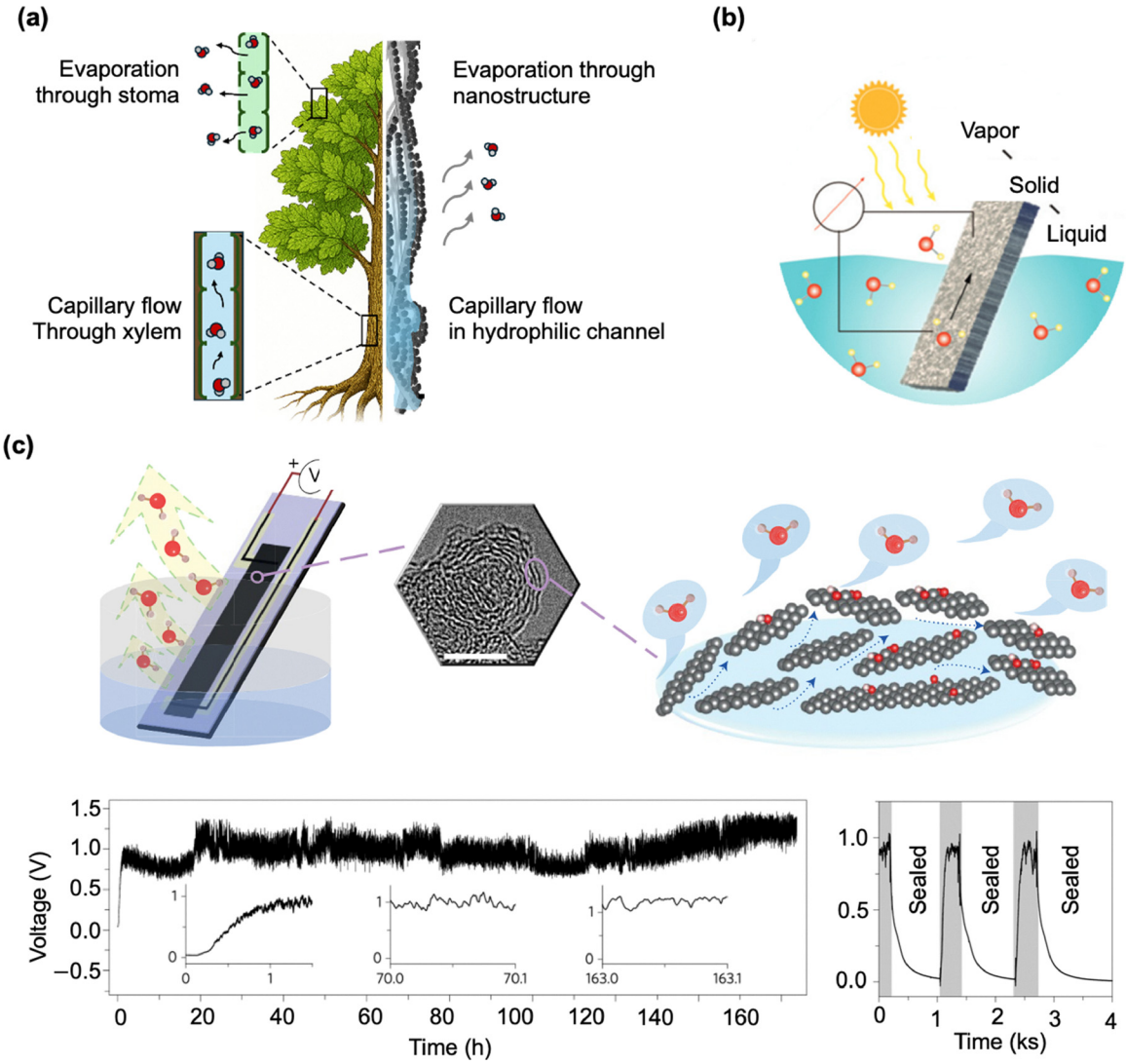

Fig. 2 Emergence of transpiration-inspired electricity harvesting enabled by hydrophilic micro-/nano-capillary architectures. (a) Analogy between natural transpiration and "artificial tree" devices used for electricity generation. The left schematic depicts water uptake and ascent through xylem and evaporation through stomata, the two functional elements most directly emulated in TIH. The right schematic illustrates how hydrophilic channels can replace xylem, while nanostructured media at an exposed surface sustain evaporation in a stomata-like manner. (b) Schematic illustration of a transpiration-inspired hydrovoltaic (TIH) device. Liquid water wicks through a hydrophilic porous matrix and evaporates to vapor at the exposed interface; electrodes placed at two ends across the solid matrix measure a voltage and sustain an electric current through an external circuit. Reproduced with permission.[5] Copyright 2022, Royal Society of Chemistry. (c) Representative TIH implementation using nanostructured carbon. A carbon-black film (black region) deposited on a substrate (blue) comprises interconnected nanopores (TEM image). Upon partial immersion, water infiltrates the porous network and continuously evaporates from exposed regions, producing a sustained electrical output (bottom left). Sealing the device suppresses evaporation and extinguishes the voltage (bottom right), supporting an evaporation-sustained generation mechanism. Reproduced with permission.[20] Copyright 2017, Springer Nature.

and the evaporating region, reflecting the coupling of flow, ion redistribution, and interfacial charge separation along the porous pathway.

3.2 Early demonstrations and electrokinetic interpretation

One of the early demonstrations of HV power generation was reported in 2017 by Xue *et al.* using a nanostructured carbon device. In their approach, a carbon-soot film was deposited on a glass substrate (for example, by ethanol-flame deposition), rendered hydrophilic, and connected by carbon nanotube electrodes near its top and bottom edges.[20] When the bottom edge was submerged in deionized water, capillary infiltration through the nanoporous network drew liquid upward, while evaporation to air sustained the flow. This, in our view, closely mirrors the functional logic of plant transpiration, at least in part. The device produced an output on the order of volts and maintained a stable signal for extended operation, reported to exceed 160 hours. A particularly informative observation was the strong dependence on evaporation. When evaporation was suppressed (for example by sealing the system so that local

relative humidity approached 100%), the voltage rapidly vanished. When the system was reopened and evaporation resumed, the output was restored. This reversibility directly implicates evaporation as essential not only for initiating but also for maintaining steady power generation.

Mechanistically, the original interpretation invoked classical electrokinetic concepts, such as streaming current and streaming potential, which naturally connect pressure- or capillarity-driven flow in charged confinement to an electrical potential difference. At the same time, the detailed physics remained incompletely resolved. Around the same period, Liu, Kunai and co-workers reported evaporation-driven electricity generation in single-walled carbon nanotube devices using polar organic solvents such as acetonitrile[41] and alcohol.[42] Although such solvents are less ubiquitous than water, these studies were valuable in shaping early mechanistic thinking and highlighting the importance of liquid saturation asymmetry in evaporation-driven power generation.[43] Subsequent studies have shown that multiple mechanisms can contribute, depending on material composition, pore morphology, ionic strength, and whether the device operates in a sustained-flow regime or a transient wet–dry asymmetry regime. We summarized several key mechanisms proposed in the following section.

4. Mechanism of electricity transduction in TIH devices

4.1 Electrokinetic mechanisms

4.1.1 Electric double layer formation at charged solid–electrolyte interfaces. Several theoretical frameworks have been proposed to describe electricity generation in TIH devices. Despite differences in emphasis, most models share a common electrokinetic foundation: formation of an electric double layer (EDL) at the interface between a charged solid surface and an electrolyte.[44] Many solids acquire surface charge through ionization of functional groups or specific ion adsorption; in plants, xylem walls are typically negatively charged. The resulting interfacial charge attracts counterions and repels co-ions, producing an asymmetric ion distribution near the surface. The EDL is commonly described as a compact Stern layer, where counterions are strongly associated with the surface, and a diffuse layer, where counterions extend into the solution with weaker association.

When capillary pressure (or other pressure gradients) drives liquid through a charged micro- or nanochannel, counterions in the diffuse layer are advected along the channel. This selective interfacial ion transport can generate an axial electric field and a potential difference between channel ends. How that ionic motion is converted into a sustained electronic current depends on the detailed device properties and architecture: whether charge conversion occurs primarily at electrodes through faradaic reactions across an electrically insulating substrate, within an electronically conductive porous solid, or through interfacial coupling to carriers in a semiconducting material (Fig. 3).

4.1.2 Streaming potential from pressure-driven EDL transport across electrically insulating substrates. Among the electrokinetic explanations proposed for TIH devices, the most established is the classical streaming potential mechanism.[45–48] In this framework, pressure-driven flow through a charged channel convects excess countercharge in the diffuse layer, producing an ionic streaming current; under open-circuit conditions, charge separation builds an opposing electric field that yields a measurable streaming potential. Formally, the phenomenon is captured by coupled continuum descriptions of flow and charge transport (for example, Navier–Stokes/Stokes for hydrodynamics coupled with Poisson–Nernst–Planck for electrostatics and ion migration), which together describe how interfacial charge, flow, and ionic flux co-evolve in confined electrolytes.

As liquid moves through a charged channel, the net charge density in the diffuse layer is advected, producing the ionic streaming current I_{str}:

$$I_{str} = \int_{-R}^{R} \rho_e(r) v_x(r) \mathrm{d}r \tag{8}$$

where $\rho_e(r)$ is the local volumetric charge density in the EDL, $v_x(r)$ is the axial velocity profile, and R denotes the characteristic radial length scale of the channel. A defining assumption of the classical picture is that the channel walls are electrically insulating, so the convected ionic current cannot, by itself, constitute a sustained electronic current through an external circuit. Instead, conversion between ionic and electronic current must occur through faradaic charge-transfer reactions at the electrodes (often implemented using redox couples such as Ag/AgCl). If the external circuit is open (or highly resistive), continuous faradaic conversion is impeded. Charge therefore accumulates, building an electric field along the channel that drives an opposing, field-driven ionic current typically described as a conduction current I_{cond}:

$$I_{cond} = \int_{0}^{R} \kappa \mathrm{d}r \tag{9}$$

where κ is the electrolyte conductivity. At steady state under open circuit conditions, the currents balance, $I_{str} + I_{cond} = 0$, and the resulting streaming potential satisfies:

$$V_{str} = I_{str} R_{solution} \tag{10}$$

where $R_{solution} = \kappa^{-1}$ is the effective solution resistivity. Applying the parallel-plate approximation (and under standard electrokinetic assumptions), this reduces to the familiar relation:

$$V_{str} = \frac{\varepsilon_0 \varepsilon_r \zeta}{\mu \kappa} \Delta p \tag{11}$$

where $\varepsilon_0 \varepsilon_r$ is the electrolyte permittivity, ζ is the zeta potential, μ is the viscosity, and Δp is the pressure drop along the channel. Eqn (11) yields several core design intuitions relevant to TIH. First, V_{str} increases with stronger interfacial charge (larger ζ) and larger driving pressure Δp. In TIH devices, Δp is often supplied by capillary pressure, which increases as the characteristic pore radius decreases (eqn (1)). This coupling suggests that smaller pores can, in principle, support larger streaming

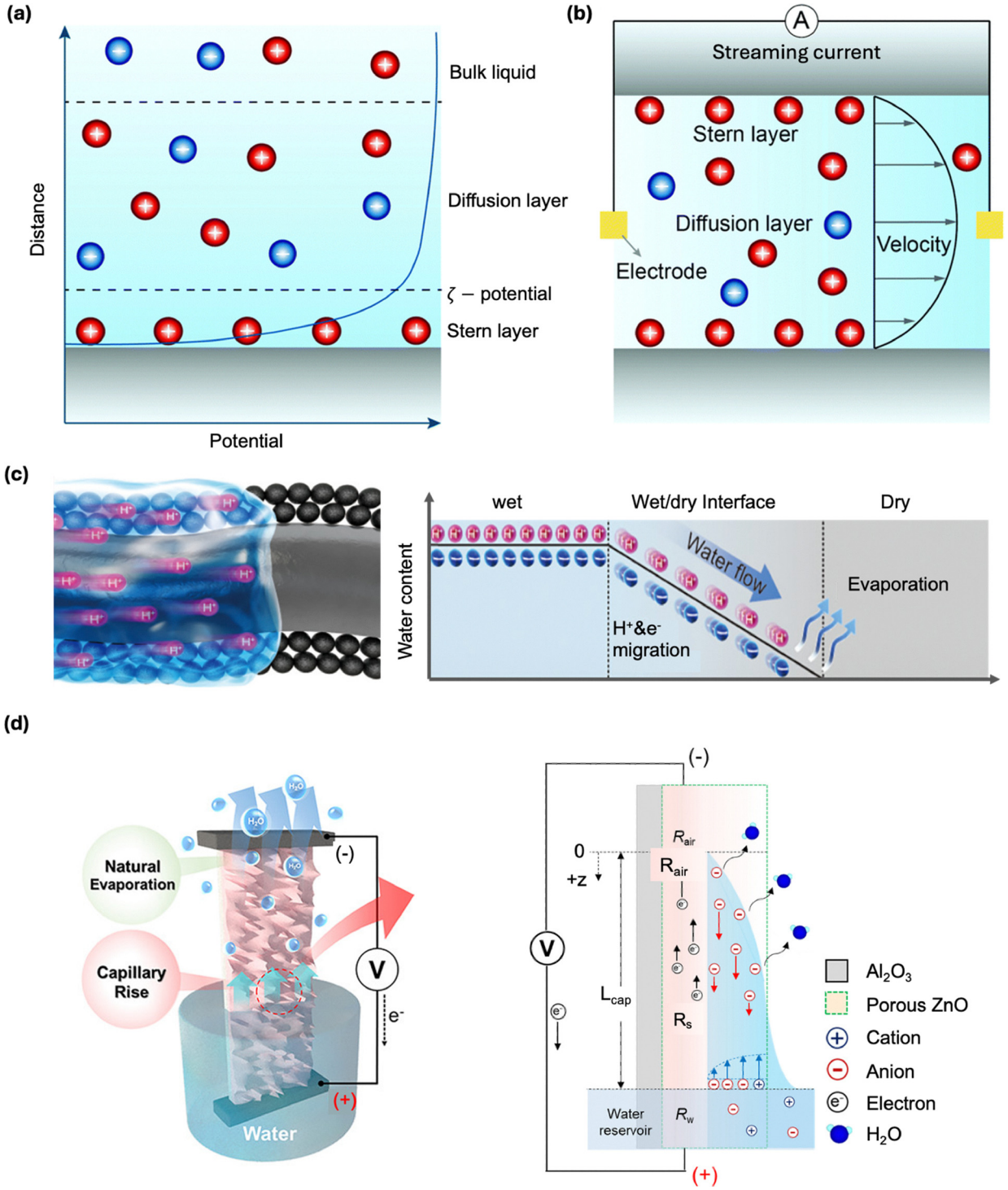

Fig. 3 Electrokinetic routes for electricity generation in TIH devices. Mechanisms are grouped into three conceptual classes: classical streaming, pseudo-streaming in conductive porous channels, and ionovoltaic transduction in semiconducting frameworks. (a) and (b) Electric double layer (EDL) at a negatively charged solid surface (grey) and the classical streaming-current/streaming-potential mechanism. Cations and anions are shown as red and blue circles, respectively; the blue curve denotes the electrostatic potential *versus* distance from the surface. Reproduced with permission.[5] Copyright 2022, Royal Society of Chemistry. (c) Pseudo-streaming (PS) mechanism in an electronically conductive porous medium. Protons (red) and electrons (blue) are depicted schematically; conductive carbon-black nanoparticles (black) are deposited on a hydrophilic cellulose fabric. Water infiltration and evaporation (white–blue arrows) are proposed to couple interfacial ion motion to electron transport within the percolated carbon network. Reproduced with permission.[21] Copyright 2019, American Chemical Society. (d) Ionovoltaic mechanism. In contrast to the PS picture, a diffusion/electrodiffusion flux opposing the convective ion transport (analogous to the conduction current in classical streaming) is proposed to drive an electronic response in the solid *via* interfacial Coulombic coupling. Reproduced with permission.[22] Copyright 2019, American Chemical Society.

potentials, provided that the channel remains sufficiently permeable to sustain flow. Second, V_{str} decreases with increasing electrolyte conductivity κ, a trade-off that is closely related to EDL screening. At higher ionic strength, the Debye length shrinks to the nanometer scale, compressing the diffuse layer and reducing the degree of counterion selectivity within the channel, thereby suppressing streaming-potential generation.[49] Consistent with this expectation, Xue *et al.* reported a decrease in voltage at higher salt concentrations and attributed the trend to Debye screening that weakens EDL-mediated selective ion transport.[20] In TIH, evaporation does more than initiate capillary uptake: it continuously maintains a pressure gradient (and thus Δp) by sustaining capillary replenishment, analogous to transpiration in plants. Within the classical electrokinetic streaming framework, evaporation therefore stabilizes Δp, supporting a persistent I_{str} and a sustained V_{str}, so long as a stable wetted pathway and interfacial charge are maintained.

A key caveat, however, is that the classical streaming-potential mechanism is fundamentally formulated for insulating channels and typically presumes electrode redox chemistry to close the circuit and convert ionic current into electronic current. Many TIH reports instead employ electronically conductive porous networks (for example, carbon-based films) and observe sustained current output without explicit redox couples. These observations motivate ''modern'' alternative mechanisms in which the conductive channel itself participates in charge transport and the coupling between ionic motion and electronic carriers becomes essential, which we discuss next.

4.1.3 Pseudo-streaming in electronically conductive porous channels. To rationalize sustained current generation in hydrovoltaic devices that lack explicit redox couples, Kim and co-workers proposed a pseudo-streaming (PS) mechanism in which electronic carriers in a percolated conductor migrate in response to ion motion within the EDL. In their 2019 study using a carbon black–coated cotton fabric, the authors argued that voltage generation is primarily interfacial, whereas current generation is transport-driven.[21] Specifically, spontaneous adsorption of cations onto the negatively charged carbon surface was proposed to establish a built-in potential that can be approximated using a Stern-layer parallel plate capacitor model:

$$V_{EDL} = \frac{\delta\sigma}{\varepsilon_0\varepsilon_r} \quad (12)$$

where V_{EDL} is the built-in voltage induced by adsorbed ions, δ is the Stern-layer thickness, and σ is the effective surface charge density. Their solvent controls supported the role of ionizable species: protic liquids produced voltage, whereas a polar aprotic solvent (propylene carbonate) produced no signal unless LiCl was added, implicating ions and their interfacial organization as essential.

Within this framework, current arises when capillary-driven wetting produces a spatially localized EDL and simultaneously drives ion transport. As the wetting front advances through the porous conductor, counterions in the diffuse layer are advected; electrons in the conductive carbon network are proposed to migrate in response, preserving local electroneutrality and producing a measurable current. They termed this output a pseudo-streaming current I_{pst} because, according to their interpretation, its direction is opposite to that expected for the classical streaming current under comparable pressure-driven flow in capillaries of the same sign of surface charge. This directional distinction was presented as an experimentally falsifiable feature that could help discriminate between pseudo-streaming and classical streaming behaviors across different systems.

Sustained voltage in the PS picture requires spatial asymmetry in wetting: one end of the device is wetted and supports EDL formation and ionic transport, whereas the opposite end remains comparatively dry and lacks a comparable interfacial ionic structure. This wet–dry asymmetry creates a potential difference between the two ends and persists only while the asymmetric state is maintained. If the porous network becomes uniformly wetted, the EDL-related potentials at the two electrodes are expected to equilibrate, and the voltage collapses. Evaporation plays a stabilizing role by continuously removing water from regions away from the wetting site, thereby helping maintain the spatial potential gradient and enabling longer-lived output under ambient conditions.

A qualitative scaling relation for the pseudo-streaming current has been suggested:

$$I_{pst} \propto Q\sigma s \quad (13)$$

where Q is the flow rate and s is a characteristic separation length capturing the spatial extent of wet–dry asymmetry and/or charge separation.[50] This form captures intuitive dependencies, namely that stronger capillary transport (larger Q) and stronger interfacial charge (larger σ) should increase the current magnitude, suggesting design routes that increase hydrophilicity, reduce flow resistance, and enhance surface ionization. However, the relation remains phenomenological. A quantitative framework that couples partially saturated flow, evolving EDL structure, and the simultaneous ionic and electronic conductivities of the porous conductor is still needed to predict how I_{pst} and the associated voltage scale with pore geometry, electrolyte composition, and evaporation rate.

4.1.4 Ionovoltaic mechanisms in semiconducting channels. A complementary class of mechanisms emphasizes coupling between evaporation-driven ionic polarization in the liquid and charge carrier transport in semiconducting solids. In 2019, Yoon *et al.* introduced an ionovoltaic mechanism, in which evaporation-driven ionic accumulation generates a local electric field that modulates carrier transport within the solid channel.[22] The central idea is that ion accumulation near the evaporating edge polarizes the electrolyte, and the resulting field drives an electronic response in the semiconducting framework through Coulombic coupling at the solid–liquid interface. In their initial demonstration using aluminium-doped zinc oxide (ZnO:Al), the positively charged surface preferentially attracts anions. Capillary flow convects anions upward (I_{conv}, blue arrow in the schematic), while evaporation enriches ions near the capillary edge, producing spatial ionic polarization. This polarization generates a local electric field along the ZnO channel that drives an opposing diffusion or electro-diffusion flux I_{diff} (red arrow), conceptually

analogous to the counter-current that balances convection in classical streaming. Through interfacial Coulombic interactions, the anion back flux I_{diff} is proposed to induce a compensating electronic response in the semiconducting channel to maintain local electroneutrality, giving rise to an electronic current I_s (measured as the device output). An Ohmic relationship between measured current and voltage was reported, $V_s = I_s R_s$, where R_s is the effective electrical resistance of the ZnO channel.

Subsequent work extended this concept to other materials. In 2021, the same group reported supporting evidence using SiO_2 and MoS_2 nanoflake channels.[51] Because their surfaces are negatively charged, cations are selectively transported, and the output polarity reverses relative to ZnO:Al. To probe ion enrichment directly, NaCl was added and the spatial sodium distribution was quantified by X-ray photoelectron spectroscopy (XPS), revealing a stronger Na signal near the upper region of the device, consistent with evaporation-driven accumulation at the capillary edge. On this basis, the authors argued that continuous evaporation maintains localized enrichment, sustaining an electric field and a dynamic balance between convective transport and back-diffusion that continuously couples to electronic transport in the semiconducting network.

Conceptually, ionovoltaic and pseudo-streaming mechanisms share a common theme: ionic motion in the liquid couples to electronic current in the solid. The proposed driving force for the electrical current, in the case of ionovoltaics, is an evaporation-sustained electric field arising from ion accumulation and concentration gradients along a semiconducting channel. Although spatial ion enrichment has been experimentally observed, a major gap remains in a quantitative framework that links the measured ionic concentration profile (and its evolution under evaporation) to the resulting electric field and to the magnitude and scaling of I_s and V_s along the channel.

4.2 Importance of evaporation

Beyond sustaining continuous operation, multiple studies suggest that evaporation can also increase the magnitude of the voltage and current produced by TIH devices. In other words, evaporation can act not only as the engine that maintains capillary replenishment, but also as an effective amplifier of the electrical output (Fig. 4).

Youm *et al.* examined this effect using a carbon black coated cellulose acetate microfiber cylindrical generator.[26] Carbon black nanoparticles were deposited onto a porous cellulose microfiber cylinder to form the active HV element, and electrodes were attached at both ends. A water droplet delivered near the positive electrode initiated infiltration and capillary-driven transport through the porous network, establishing a longitudinal wetting gradient along the cylinder. Using a streaming-potential framework with empirical pore-scale parameters (including an average pore size), the authors estimated an open-circuit voltage of approximately 75 mV. To isolate the role of evaporation, the device was first sealed to suppress water loss. Under sealed conditions, the measured voltage was about 120 mV, broadly consistent with the estimate given the uncertainties associated with pore geometry, surface charge, and effective conductivity in a heterogeneous porous medium. Strikingly, when the device was unsealed and evaporation was permitted, the open-circuit voltage increased to approximately 310 mV, nearly three times higher than the sealed value. This result indicates that evaporation does more than sustain flow: it can intensify the interfacial and transport conditions that generate a potential difference, for example by maintaining a larger effective pressure drop, sharpening spatial ion distributions near the evaporating region, and/or stabilizing wet–dry asymmetry along the device. Accordingly, the measured voltage was expressed as the sum of a streaming contribution and an evaporation-associated contribution:

$$V_{OC} = V_{str} + V_{evap} \quad (14)$$

where V_{OC} represents the open-circuit voltage measured experimentally, V_{str} is the streaming potential calculated using eqn (11), and V_{evap} denotes the additional voltage attributed to evaporation. The authors further related V_{evap} to an

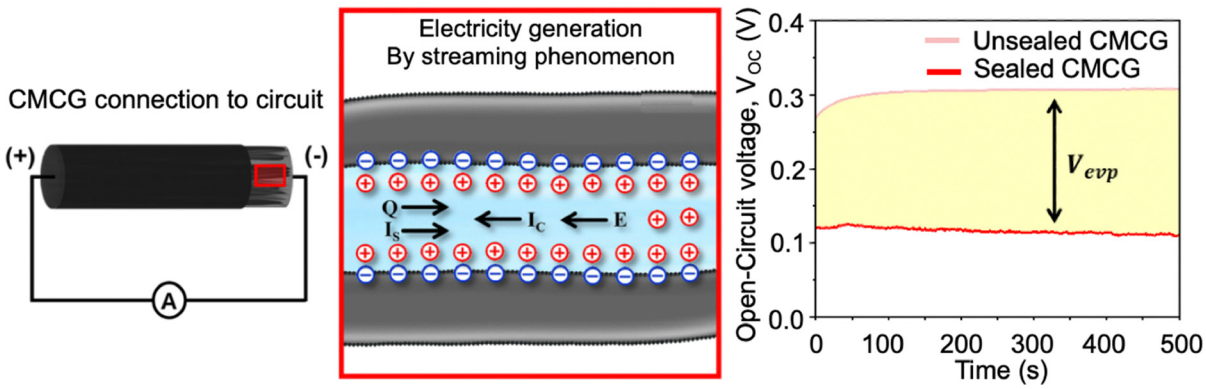

Fig. 4 Role of evaporation in enhancing TIH power output. Left, circuit schematic for the cellulose microfiber cylindrical generator (CMCG). The dark region denotes the wetted segment, whereas the shaded region denotes the comparatively dry segment, establishing a longitudinal wet–dry asymmetry. Middle, microscopic view of the streaming-current framework: capillary-driven flow Q advects excess countercharge to generate a streaming current I_s; the induced electric field E drives an opposing conduction current I_c. Right, measured open-circuit voltage under sealed (evaporation suppressed) and unsealed (evaporation allowed) conditions; V_{evp} denotes the voltage increment associated with evaporation. Reproduced with permission.[26] Copyright 2023, Elsevier.

evaporation-associated power density W by invoking the latent heat of vaporization F and the mechanical work associated with liquid evaporation ω:[3]

$$W = \frac{F\omega}{L} \quad (15)$$

This expression is heuristic and does not, by itself, provide a direct route to predict the voltage magnitude from independently measurable transport parameters. Nevertheless, the qualitative conclusion is robust: evaporation can measurably boost hydrovoltaic output. This is reminiscent of transpiration in trees, where evaporation at leaves generates strongly negative water potentials that both sustain and intensify long-range transport. Taken together, these observations reinforce the conceptual alignment between plant hydraulics and TIH operation. Evaporation sustains device function and, in some architectures, measurably enhances performance. This perspective motivates the comparisons developed in the following sections, where we examine how macroscopic geometry, pore-scale structure, and environmental conditions that govern transpiration in trees similarly regulate output in TIH systems, and how these insights can be used to improve power-generation efficiency.

5. Macroscopic geometric variables that shape TIH performance: length, thickness, and width

It is estimated that ~73 000 tree species exist worldwide.[52] Owing to differences in genetics, climate, competition for light and space, water availability, and soil quality, trees exhibit a wide range of macroscopic geometries, most notably in height and trunk diameter.[53–55] These geometric differences directly shape the physics of water transport. Greater height can confer improved access to sunlight and thus enhance photosynthetic potential. However, increasing height also imposes a larger gravitational head and requires the maintenance of more negative water potentials at the crown to sustain sap ascent through xylem. In general, xylem water potential decreases approximately linearly with tree height and can reach values as low as −2 MPa.[56] This trend is broadly observed across major tree groups, including both angiosperms and gymnosperms.[57] Under such extreme tension, the likelihood of cavitation increases, particularly under water deficient conditions such as drought or during daytime exposure to intense sunlight and elevated temperatures. Cavitation can lead to hydraulic failure and, ultimately, mortality, thereby imposing a fundamental limit on upward growth. Furthermore, increasing tree height demands a mechanically stronger xylem network to support trunk mass against gravity, indicating that both cavitation resistance and structural stability constrain how negative xylem pressures can become.[37,58] To mitigate cavitation risk arising from highly negative water potentials and limited sap availability, tall trees may reduce transpiration through stomatal closure, while hydraulic resistance also naturally increases along longer xylem pathways, slowing flow and reducing the rate of water loss.[59] In parallel, trees achieve mechanical stability through trunk thickening, which not only provides structural reinforcement but also increases hydraulic capacitance and internal water storage, thereby buffering transient imbalances between water supply and evaporative demand (Fig. 5).[60]

At the same time, water availability, water potential, and tree size significantly influence rooting depth and lateral root spread.[61,62] In water-rich environments with high precipitation, roots often expand both deeper and farther laterally because water and nutrients can be accessed from multiple soil layers. This favorable water supply promotes increases in both height and girth, which in turn require a more extensive root network to provide greater water uptake and mechanical anchoring. A larger root system also improves soil reinforcement, helping

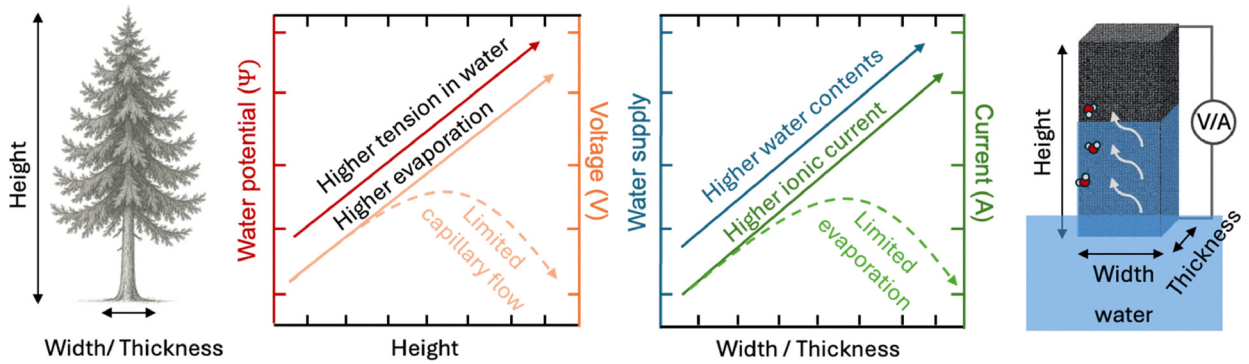

Fig. 5 Linking macroscopic substrate geometry to liquid transport in trees and TIH devices. In trees (left), height sets the gravitational component of water potential and increases hydraulic resistance, requiring more negative potentials at the crown to sustain ascent. In TIH devices (right), increasing the vertical length can increase cumulative evaporation and the resulting electrokinetic migration, often increasing the measured voltage; however, excessive evaporative demand can outpace capillary replenishment, induce partial drying, and suppress output. In trees, trunk diameter (width) reflects both mechanical stability and hydraulic capacity. In TIH devices, width and thickness (lateral dimensions) set the number of parallel flow pathways and interfacial area available for ion transport, typically increasing current. Yet if the device becomes too thick, evaporation-driven throughflow can be hindered by longer diffusion paths and increased internal flow resistance, reducing current despite a larger cross-sectional area.

prevent uprooting under gravitational and wind loading. In contrast, trees in arid climates adopt a wider range of rooting strategies depending on species.[63] For example, phreatophytes develop deep roots that can access groundwater, allowing them to maintain high transpiration rates. On the other hand, cacti typically form shallow but laterally extensive root systems that maximize the capture of episodic surface moisture, while minimizing water loss through strong suppression of the leaf area. Taken together, species identity, water availability, gravity, cavitation risk, and material strength collectively bound attainable macroscopic size and form, confining extreme tree heights to a narrow hydraulic operating envelope.

A closely related geometry–transport coupling appears in transpiration-inspired hydrovoltaics (TIH), which can be viewed as engineered, electricity-generating analogs of trees. In TIH devices, macroscopic dimensions do not simply define electrode spacing or active area; they also regulate the balance among capillary replenishment, evaporative demand, and internal flow resistance. Together, these factors determine the saturation profile and the interfacial conditions required for electrokinetic transduction. As a result, device length often correlates with voltage output, whereas width and thickness more strongly influence current by increasing the number of parallel flow pathways, wetted interfacial area, and overall liquid throughput. These trends, however, are not universal and may reverse depending on material properties and on whether the dominant transduction mechanism is electrokinetic streaming (for dielectric capillaries), pseudo-streaming (for electrically conductive capillaries), or ionovoltaic coupling that is often seen inside semiconducting channels.

5.1 Effect of device length on power output

A frequently reported trend is that open-circuit voltage increases with device length, whereas short-circuit current exhibits a nonmonotonic (volcano-shaped) dependence on length.[20,64–70] In a representative study, Li *et al.* printed vermiculite, a layered mineral with strong ion-selective properties, onto quartz.[64] The stacked flake morphology formed parallel nanochannels that supported selective cation transport. Increasing the channel length from 2 to 3 cm increased the open-circuit voltage from ~0.75 V to nearly 1.0 V. By contrast, the short-circuit current increased from ~40 nA at 1 cm to ~50 nA at 2 cm but decreased upon further length extension (Fig. 6a).

Li *et al.* interpreted the output within a streaming-potential framework. The observed length dependence, however, highlights a practical limitation of applying classical streaming theory directly to evaporatively driven TIH devices. In the classical expression (eqn (11)), V_{str} depends on the driving pressure drop Δp but does not explicitly depend on the channel length. Moreover, for idealized channels, the streaming current can be expressed in a form proportional to the pressure gradient:

$$I_{str} = \int_{-R}^{R} \rho_e(r) v_x(r) dr = \frac{\varepsilon_r \varepsilon_0 r^2 \zeta}{\mu} \frac{\Delta P}{L} \quad (16)$$

where r is the pore radius and L is the channel length. If other parameters are held constant and ΔP is fixed, increasing L reduces

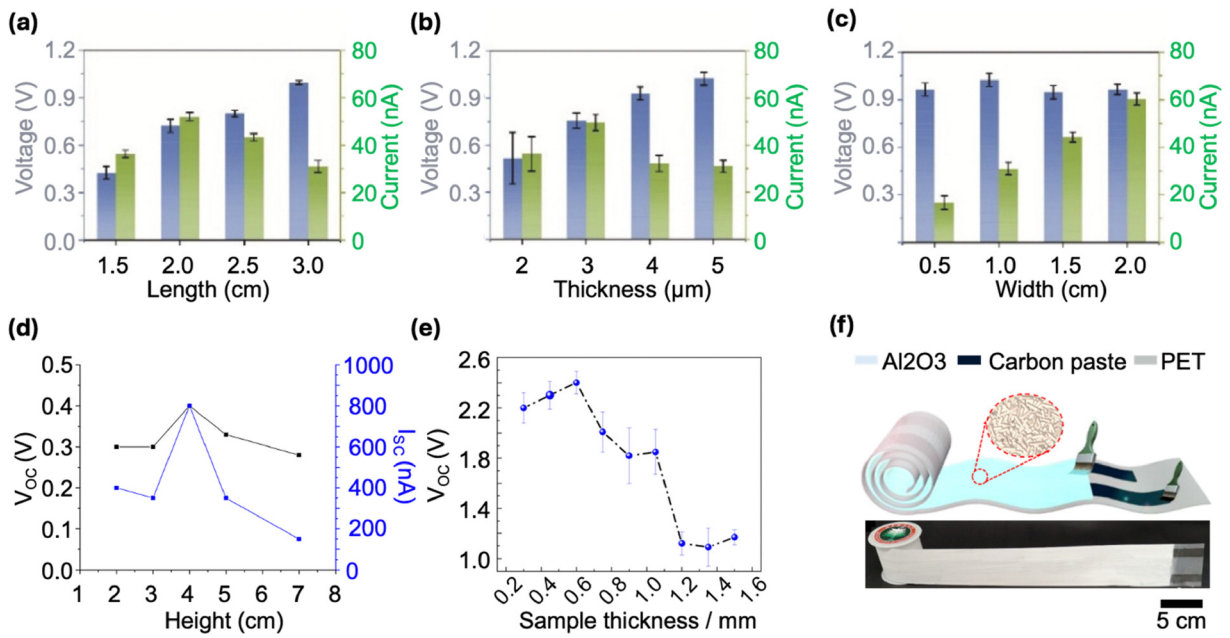

Fig. 6 Device dimensions, output trends, and scaling strategies guided by geometry–performance relationships. (a)–(c) Voltage and current *versus* length, thickness, and width for a vermiculite-based TIH device. Reproduced with permission. Copyright 2023, Elsevier.[64] (d) and (e) Voltage and current *versus* height and thickness for the Al_2O_3-based device, highlighting non-monotonic behavior arising from the competition between the evaporation rate and capillary replenishment. Reproduced with permission.[49] Copyright 2022, American Chemical Society. (f) Scaled-up TIH system on a flexible PET substrate with deposited Al_2O_3 and carbon-paste electrodes, demonstrating a practical route to increase current by increasing the effective lateral area and parallel pathways. Reproduced with permission.[71] Copyright 2019, American Chemical Society.

the pressure gradient $\Delta P/L$ and therefore decreases I_{str}, opposite to the initial increase observed experimentally. This discrepancy suggests that under evaporative operation, ΔP, saturation state, and effective transport parameters (for example, permeability, conductivity, and interfacial charge regulation) are not invariant with length.

A useful way to reconcile these discrepancies is to treat evaporation as the missing coupling between geometry and driving forces. For instance, Li *et al.* proposed that longer channels can sustain greater cumulative evaporation, which strengthens capillary replenishment and amplifies charge separation along the vermiculite surface up to an optimal length. Beyond this threshold, distributed evaporation promotes partial drying and increases internal flow resistance, leading to continued voltage growth but reduced current.

5.2 Effect of device thickness: voltage enhancement and nonmonotonic current

By varying the number of coating cycles, Li *et al.* tuned the thickness of the vermiculite film. The output voltage increased with thickness, whereas the current increased to a maximum and then declined (Fig. 6b). The authors proposed that thicker films can sustain a larger "charge imbalance," resulting in higher voltage, but that excessive thickness increases internal flow resistance and reduces evaporation, impeding ion transport and lowering current.

5.3 Effect of device width: weak voltage dependence and increased current

When Li *et al.* increased the film width at fixed length and thickness, the voltage remained nearly constant, while the current increased approximately proportionally (Fig. 6c). This scaling is consistent with width primarily adding parallel pathways: increasing width increases cross-sectional area for water and ion transport (and often the total wetted interfacial area), thereby increasing current. Because width does not substantially change the longitudinal transport distance between electrodes, it has a weaker effect on the axial gradient that sets the potential, and the voltage can remain largely unchanged.

5.4 Deviations in geometry dependence across the literature

The relationship between channel length and voltage generation is not universally monotonic.[49,72–74] For example, Chaurasia *et al.* coated Al_2O_3 nanoparticles onto a substrate and operated the HV device in deionized water.[49] Both open-circuit voltage and short-circuit current increased with length up to 4 cm but declined sharply beyond that value (Fig. 6d). The authors attributed this decline to an evaporation–replenishment mismatch: beyond an optimal length, evaporation depletes the capillary-supplied water film faster than it can be replenished, thinning or breaking the continuous wetted pathway needed for ion transport and EDL formation near the upper electrode. In this regime, both the electrokinetic driving and the effective conductivity deteriorate, reducing voltage and current. Chaurasia *et al.* also reported a thickness dependence that differed from the vermiculite system (Fig. 6e). After an initial increase in voltage as the thickness increased from 0.2 to 0.6 mm, both voltage and current decreased with further thickness increase. They again invoked evaporation–transport coupling, proposing that thicker Al_2O_3 layers hinder evaporation and water transport, thereby weakening interfacial gradients and reducing the potential difference between electrode regions.

Across the literature, such discrepancies are expected to be material- and morphology-dependent, reflecting differences in porosity, tortuosity, wettability, surface charge regulation, water retention, and the relative magnitudes of ionic and electronic conductivities. Despite these variations, a consistent physical theme emerges. Evaporation both drives flow and helps maintain the interfacial asymmetries that enable charge separation and ion transport. Under moderate conditions, stronger evaporation can enhance output. Once evaporation exceeds a critical threshold relative to capillary replenishment, partial drying and increased resistance suppress transport and degrade performance. At present, however, there is no quantitative framework that directly links evaporation dynamics and saturation profiles to electrokinetic source terms and internal resistances, and the community relies on qualitative explanations even when observed trends differ.

Fortunately, the role of evaporation is well understood in natural transpiration systems, where it generates negative pressure to drive water transport. Taller trees require more negative water potentials, but this requirement is bounded by cavitation risk and hydraulic conductivity. Larger trunk diameters improve mechanical support and storage but increase the water demand needed to sustain the vascular network. By benchmarking this balance between water transport and structural dimensions in trees, a deeper understanding of how evaporation influences electrokinetic phenomena, and how water–solid interactions vary across different materials will be essential to elucidate the relationship between geometric dimensions and power output in TIH devices.

5.5 Coupling of geometry and interfacial electrokinetics to maximize TIH efficiency

Building on these geometric effects, several studies have explored scaling strategies to increase hydrovoltaic output.[71,75–78] Shao *et al.* deposited Al_2O_3 nanoparticles on a flexible PET substrate to fabricate a rollable TIH device (Fig. 6f).[71] A 4 cm × 4.5 cm sample produced ~2.5 V and 200 nA. Increasing the device width to 18 cm increased the output current to ~800 nA, demonstrating scalable current generation *via* lateral expansion. Although only the width was varied in this study, the results highlight the promise of large-area manufacturing. A more quantitative understanding of evaporation-driven electrokinetics should enable predictive scaling of length and thickness as well, improving both absolute output and overall energy-conversion efficiency.

6. Microscopic variables that affect TIH performance: channel conformation and alignment

Plants sustain transpiration by integrating hierarchical xylem architectures with strong directional anisotropy.[79–81] Gymnosperms (for example, conifers and other softwoods) rely primarily

on tracheids, which are elongated, narrow conduits that couple water transport with mechanical support. Angiosperms (hardwoods) typically exhibit more heterogeneous xylem anatomy that includes vessels, fibers, and parenchyma, enabling higher hydraulic conductivity but also introducing additional pathways for storage and regulation.[82,83] Even within a single tree, conduit diameter is not uniform. Xylem elements are generally wider near the base, where lower tension is required to sustain flow, and become narrower toward the crown, where water must be transported under more negative pressures and the risk of embolism increases. Narrower conduits at height reduce vulnerability to cavitation and help preserve hydraulic continuity, even at the cost of higher flow resistance.[84] Beyond channel diameter, plants employ structural motifs that localize and compartmentalize flow. Scalariform perforation plates and related pit structures subdivide pathways and distribute resistance, helping to limit the spread of cavitation events and maintain transport through parallel routes.[85] In this sense, plant xylem is not optimized solely for low resistance; it is optimized for sustained function under fluctuating evaporative demand, balancing throughput, safety from embolism, and spatial control of water–air interfaces.

Because TIH devices generate electricity by coupling evaporation-sustained capillary flow coupled to interfacial electrokinetics, channel architecture is a primary design variable. Pore conformation and alignment regulate (1) hydraulic conductance and the ability to sustain directional flow, (2) the extent and location of the water–air interface that sets the evaporation boundary condition, and (3) the degree of ionic selectivity and EDL overlap under confinement. In this section, we survey the most common microstructural motifs in TIH, including vertically aligned, parallel, honeycomb, random, and hierarchical architectures. For each, we summarize the reported advantages and then highlight the unresolved question that recurs across the literature: how to quantitatively connect geometry to evaporation kinetics, ion selectivity, and electrical output under controlled comparisons.

6.1 Vertically aligned channels inspired by plant vasculature

Vertically aligned microchannels are the most direct synthetic analogue of plant vasculature and have been widely explored in TIH devices.[86–89] One common strategy is to use natural wood as a template. Zhou *et al.* chemically modified beech wood with citric acid to introduce carboxyl and hydroxyl groups and increase the negative surface charge.[86] Carbon-paste electrodes supported on a PET mesh were attached to the top and bottom surfaces. When the bottom of the wood block was immersed in deionized water, capillary transport occurred through preserved xylem channels, and evaporation proceeded from the exposed top surface. Proton dissociation from carboxyl groups established EDLs, and the device produced $\sim$30 mV and $\sim$2 μA, which the authors interpreted using a streaming-potential mechanism (Fig. 7a). The intrinsic anisotropy of wood provides a clear test of the role of alignment. Rotating the block by 90° reoriented the dominant channels from vertical to horizontal, suppressing transport toward the top electrode and reducing output (voltage to $\sim$15 mV and current to below 1 μA). This comparison supports a general design principle: directional, aligned pathways increase hydraulic conductance and maintain a stable saturation gradient, which strengthens sustained ion transport and therefore electrical output.

A practical limitation of many vertically aligned systems is the evaporation boundary condition: if only a small outlet region is exposed, the effective water–air interfacial area is restricted. Some studies have therefore introduced solar irradiation or localized heating to accelerate evaporation. While these approaches can increase output, they complicate deployment by relying on external energy input and by coupling device performance to illumination or heating conditions rather than to intrinsic structural design.

6.2 Parallel nanochannels in two-dimensional materials

Parallel nanochannels assembled from two-dimensional (2D) materials provide an alternative route to strong confinement with high interfacial area.[64,70,78,90,91] Layered materials naturally form slit-like channels upon stacking, and their large specific surface area can enhance ion–surface interactions that govern EDL formation and selective transport. Yu *et al.* fabricated a composite of reduced graphene oxide (rGO) and cellulose nanofibers in which rGO nanosheets assembled into a largely parallel, layered architecture (Fig. 7b).[70] This alignment created extended nanochannels with high surface area and promoted strong ion–channel coupling. When tested in deionized water, the device generated an open-circuit voltage exceeding 0.6 V and a short-circuit current of approximately 1 μA. These results illustrate the appeal of 2D assemblies: channel alignment and surface area are built into the material platform, enabling high output in compact geometries.

6.3 Honeycomb architectures that couple evaporation area with salt tolerance

Honeycomb-like porous microstructures provide a large interfacial area and distributed pathways that can simultaneously enhance evaporation and mitigate fouling.[92,93] Wu *et al.* formed a porous rGO honeycomb by casting an rGO suspension on a cold substrate, where ice-crystal templating generated a cellular network that was retained after freeze-drying (Fig. 8a).[92] The device operated in NaCl-containing reservoirs and produced an open-circuit voltage above 0.8 V in natural seawater, maintaining output for over 240 hours. A notable advantage was resistance to salt crystallization: the honeycomb geometry suppressed salt accumulation during prolonged saline operation, whereas a control sample cast on a warm substrate formed dense rGO layers, showed substantially lower voltage, and rapidly decayed to $\sim$0 V as salt crystals formed, blocked transport, and disrupted interfacial charge separation. These results emphasize that channel confirmation should be evaluated not only by peak output, but also by operational stability. Under high salinity, maintaining open flow paths and avoiding crystallization at evaporative fronts is critical. Honeycomb microstructures offer a promising route because they distribute evaporation over many pores, reduce local supersaturation

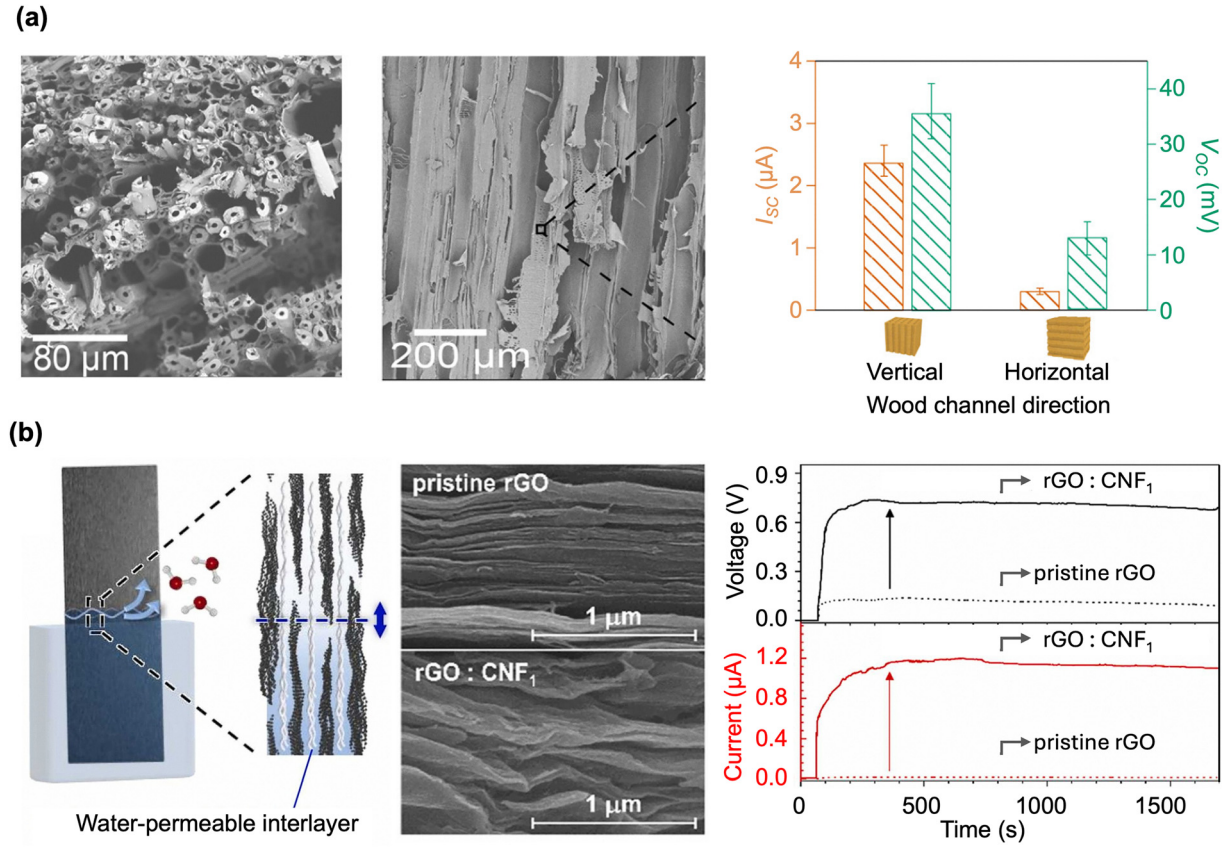

Fig. 7 Vertically and parallelly aligned channel conformations used in TIH devices and representative output characteristics. (a) Vertically aligned channels templated by natural wood. SEM images show top and side views of preserved xylem clusters; the plot compares voltage/current for devices oriented with channels vertical *versus* horizontal. Reproduced with permission.[86] Copyright 2020, American Chemical Society. (b) Parallel nanochannels in an rGO:CNF_1 composite film. The interlayer gap is larger than in pristine rGO, facilitating water transport; plots compare voltage/current of rGO:CNF_1 (solid) and rGO (dashed). Reproduced with permission.[90] Copyright 2024, Elsevier.

hotspots, and provide parallel transport routes that remain functional even if a fraction of pathways partially foul.

6.4 Random porous networks and ion selectivity through EDL overlap

Most TIH devices reported to date employ random porous networks created by packing nanoparticles without long-range alignment.[20–22,49,65,66,68,69,71–73,76,94–111] These structures are straightforward to fabricate and can deliver high output because they provide large interfacial area and nanoscale confinement. Ding *et al.* printed a toluene-soot slurry on an Al_2O_3 substrate to form a disordered carbon-black network with pore sizes spanning tens to hundreds of nanometers (Fig. 8b).[94] The negatively charged soot attracted cations from deionized water, promoting EDL formation. Importantly, under low ionic strength, a subset of pores can approach the Debye length, enabling EDL overlap that enhances selectivity by enriching counterions and excluding co-ions. The device generated an open-circuit voltage of approximately 1.0 V in deionized water. Random networks therefore illustrate a recurring trade-off in TIH: tortuosity and narrow constrictions can enhance selectivity and interfacial polarization, but they also increase hydraulic resistance and can make operation more sensitive to drying, fouling, and changes in electrolyte conductivity.

6.5 Hierarchical micro–nano structures that balance ion conductance and selectivity

Hierarchical architectures aim to combine the advantages of fast transport in larger pores with strong selectivity in smaller pores.[74,112] Wang *et al.* proposed that macropores (micrometer-scale) provide low hydraulic resistance and rapid imbibition, whereas mesopores and micropores (tens of nanometers and below) promote ion selectivity through EDL overlap (Fig. 8c).[74] In their implementation, three-dimensional hierarchically structured TiO_2 nanoflowers were grown on FTO substrates by hydrothermal synthesis, with a CNT mesh used as the top electrode. Electricity generation was probed by depositing a water droplet on the structure. By tuning precursor and HCl concentrations, the authors adjusted the pore-size distribution and observed corresponding changes in voltage and current. The design goal is explicit: couple efficient water transpiration flux with selective interfacial ion transport within a single, multiscale architecture.

6.6 Toward controlled structure–function maps for the TIH microarchitecture

Despite the diversity of channel conformations reported, there has been little systematic effort to compare architectures under

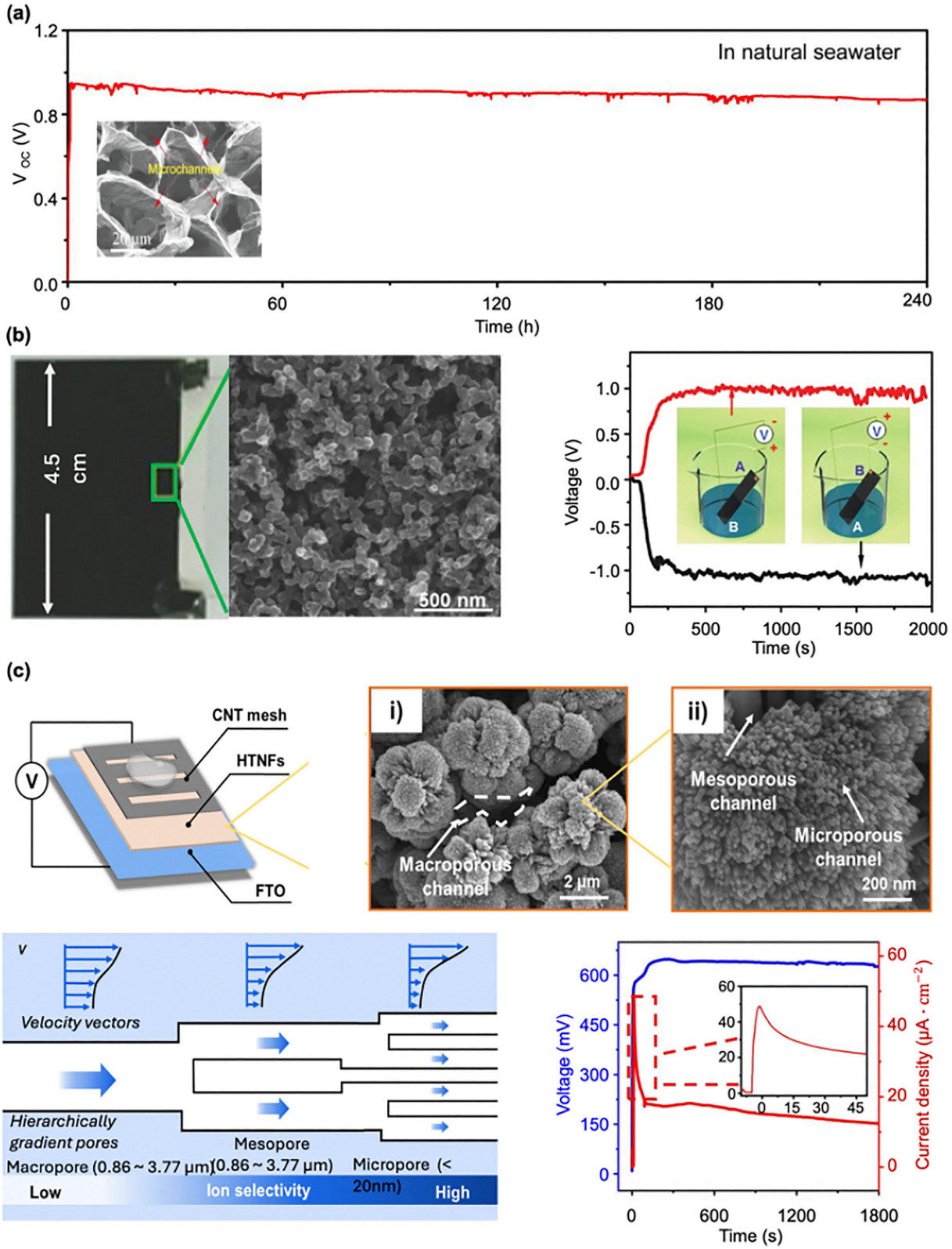

Fig. 8 Micro-, nano-, and hierarchically structured channel conformations used in TIH devices and representative output characteristics. (a) Honeycomb rGO formed by freeze-casting/freeze-drying. The cellular structure increases interfacial area and supports stable operation in saline water; the plot shows long-term voltage stability in natural seawater. Reproduced with permission.[92] Copyright 2021, American Chemical Society. (b) Random porous network formed from amorphous carbon-black nanoparticles collected from toluene soot. The left panel shows a photograph of the device (channel length ~4.5 cm). The middle panel is an SEM image highlighting the disordered porous microstructure. The right panel shows the voltage output; reversing the electrode connections flips the voltage polarity while leaving the magnitude nearly unchanged, consistent with an

interfacial origin of the signal. Reproduced with permission.[94] Copyright 2017, John Wiley VCH. (c) Hierarchical device comprising 3D dendritic TiO_2 nanoflowers, a CNT mesh, and FTO electrodes. The top-left panel illustrates the device concept. The top-middle and top-right SEM images show TiO_2 nanoflowers grown on FTO and the resulting multiscale pore network. The bottom-left schematic summarizes the hierarchical channel architecture from macro- to micropores; the blue arrow indicates the water-flow direction, emphasizing high permeability in macropores coupled with enhanced ion selectivity in micropores. The bottom-right panel reports the voltage and current–density response upon droplet addition (inset: enlarged view of the initial current peak). Reproduced with permission.[74] Copyright 2024, The Royal Society of Chemistry.

controlled conditions. In many studies, changes in microstructure are accompanied by simultaneous changes in chemistry, surface charge, conductivity, or mechanical properties, making it difficult to isolate geometric effects. As a result, even for fixed active material loading and comparable pore volume or surface area, there is no consensus on a basic design question: which channel geometry (vertically aligned, parallel layered, honeycomb, random, or hierarchical) is optimal for a given operating condition, such as across water sources spanning wide salinity ranges?

Addressing this gap will require targeted studies that decouple channel geometry, confirmation from material composition, and salinity effects across different TIH platforms. One practical approach is to fabricate families of architectures from the same material platform (or with matched surface chemistry) while independently measuring hydraulic conductance, evaporation flux, saturation profiles, and effective ionic selectivity. Linking these measurements to electrical output would enable structure–function maps that clarify how channel conformation controls (1) water transport and replenishment, (2) spatial localization of evaporation, (3) EDL overlap and ion selectivity, and (4) internal electrical resistance. Such controlled comparisons would move TIH channel design from qualitative analogy to predictive engineering, enabling architectures that are optimized not only for peak output but also for stability under real-world conditions.

7. Environmental variables that affect TIH performance: temperature, humidity, airflow, and salinity

Plant transpiration is strongly regulated by the environment.[54,113,114] Temperature, relative humidity, and solar irradiation set the evaporative demand at the leaf surface, while airflow controls convective mass transfer and therefore the evaporation flux. Because TIH devices rely on the same evaporation-sustained capillary transport to maintain interfacial ion redistribution and electrical output, these environmental variables become intrinsic ''operating conditions'' rather than external perturbations. Consistent with this coupling, many studies report pronounced changes in voltage and current when temperature, humidity, and airflow are varied, and when the device is reoriented relative to gravity and the surrounding air.[115]

In this section, we summarize the dominant environmental parameters that shape TIH performance: ambient temperature, airflow velocity, relative humidity, and device orientation. We also distinguish between continuous-flow TIH systems, where evaporation amplifies both the driving force and the electrokinetic response, and droplet-driven or pseudo-streaming systems, where evaporation primarily sets the operational lifetime rather than the output amplitude. We conclude with emerging strategies for environmentally robust architectures that maintain stable output despite ambient fluctuations.

7.1 Temperature and airflow increase TIH output by increasing evaporative demand

Several studies that have systematically examined temperature and wind effects report that both open-circuit voltage and short-circuit current increase with elevated evaporative demand.[65,76,92,105,110,116–118] Chi *et al.* tested a porous, hydrophilic Al_2O_3-based HV device with top and bottom electrodes inside a programmable chamber that enabled independent control of temperature and relative humidity.[65] Under fixed humidity, increasing temperature increased both voltage and current (Fig. 9a). The authors attributed this enhancement to accelerated evaporation, which increases capillary replenishment and strengthens the pressure and concentration gradients that drive ion transport through the micro-nanoporous network. Airflow produces a closely related effect. Increasing wind speed across the device surface increased both voltage and current (Fig. 9b), consistent with convective mass transfer: faster airflow reduces the boundary-layer thickness, increases the evaporation flux, and therefore increases the capillary flow rate needed to replenish liquid lost at the evaporating interface. In TIH devices where electrical output scales with sustained liquid or ionic transport, increased evaporation therefore amplifies both voltage and current.

7.2 Relative humidity suppresses evaporation and reduces TIH output

Relative humidity (RH) directly controls the vapor-pressure driving force for evaporation and is therefore among the most influential ambient parameters for TIH performance. Multiple reports show that sealing a TIH device, which drives the local RH toward saturation, rapidly eliminates the voltage signal, indicating that evaporation is required not only to initiate but also to sustain electricity generation.[22,64,65,91,105,116,119] Quantitative RH dependence has also been demonstrated. Yoon *et al.* fabricated a nanoporous ZnO film on an Al_2O_3 ceramic substrate and measured output as RH was varied under otherwise comparable conditions. Both open-circuit voltage and short-circuit current decreased strongly with increasing humidity (Fig. 9c). For example, the voltage dropped from $\sim$0.45 V at 30% RH to $\sim$0.2 V at 80% RH, while the current decreased from $\sim$7 nA to $\sim$3 nA over the same range. These results are consistent with suppressed evaporation at high RH, which reduces capillary-driven replenishment and weakens the

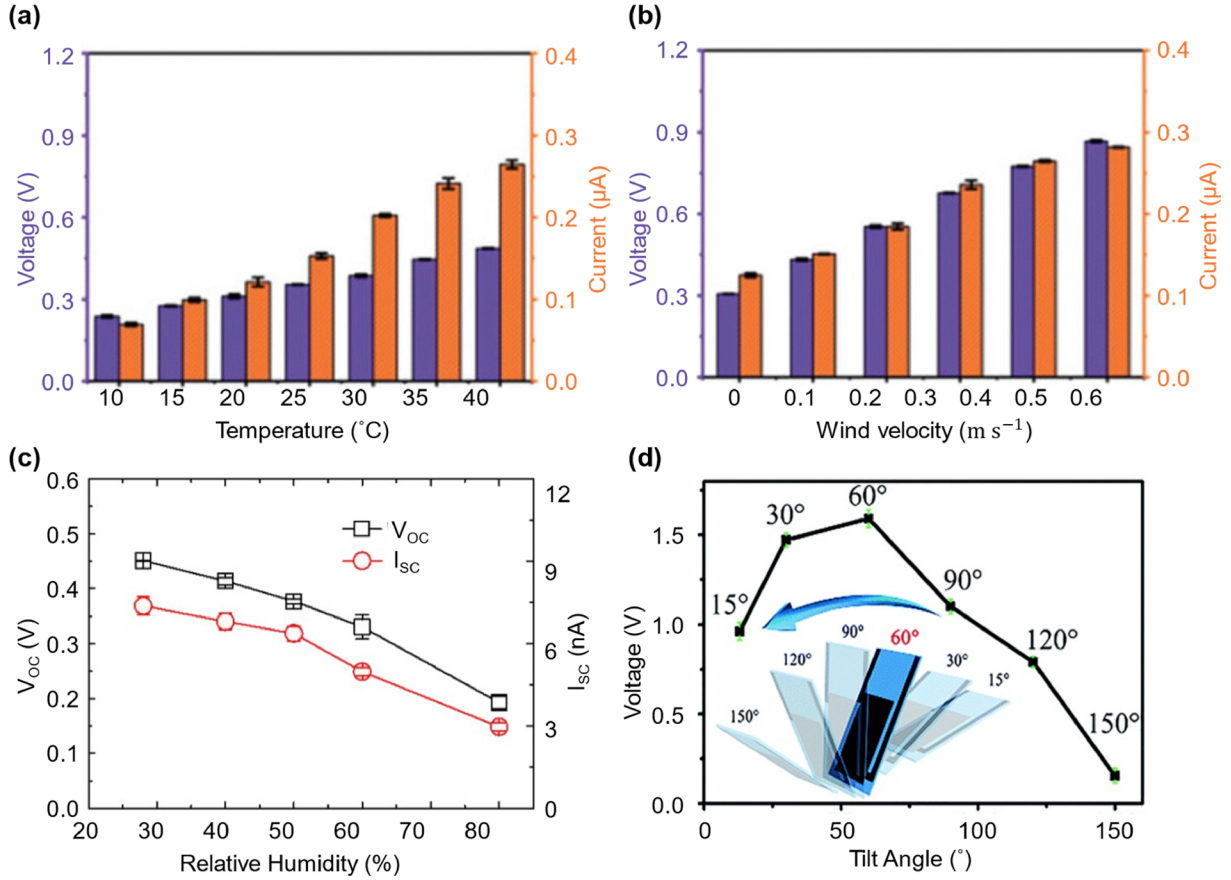

Fig. 9 Environmental control of TIH output through the evaporation rate. (a) and (b) Voltage and current *versus* temperature and wind velocity. Higher temperature and airflow increase evaporative demand and typically amplify both voltage and current. Reproduced with permission.[65] Copyright 2022, Wiley VCH. (c) Voltage and current decrease with increasing relative humidity, consistent with suppressed evaporation. Reproduced with permission.[22] Copyright 2019, American Chemical Society. (d) Voltage *versus* device tilt angle (15–150°), reflecting the balance between evaporation flux and capillary supply under gravity. Reproduced with permission.[95] Copyright 2019, Royal Society of Chemistry.

sustained ion redistribution required for EDL-mediated transduction.

7.3 Device orientation tunes the balance between capillary supply, gravity, and evaporation

The inclination angle of a TIH device can significantly affect output by changing the competition between capillary transport, gravitational drainage, and access of the active surface to air. Liu *et al.* deposited a composite film of carbon nanospheres and TiO_2 nanowires on glass, integrated a CNT electrode, and operated the device with the bottom electrode submerged in water.[95] By varying the inclination angle from 15° to 150°, they observed a pronounced angle dependence in open-circuit voltage (Fig. 9d). At low angles, capillary transport can readily drive water upward, but the evaporation boundary condition and air access may be suboptimal, limiting output. As the angle increased, voltage increased and reached a maximum (reported above 1.5 V) near 60°, consistent with an orientation that balances continuous liquid supply with efficient evaporation from the exposed surface. When the angle exceeded 90° and the active film faced downward toward the water, evaporation was strongly suppressed and the voltage decreased. This study highlights orientation as a practical design variable for field deployment. Because evaporation is also enhanced by convection, the optimal orientation may depend not only on gravity but also on the airflow direction and local wind conditions.

7.4 Effect of salinity in soil water on tree metabolism

Soil contains not only water but also a variety of dissolved ionic species such as Ca^{2+}, Na^{+}, and Cl^{-}. Because the soil water content is highly sensitive to precipitation, season, and atmospheric temperature, the salinity of water taken up by plants can fluctuate substantially. For example, during drought, elevated soil salinity can disrupt cellular osmotic balance and impair plant metabolism, ultimately reducing growth.[120,121] This phenomenon is referred to as salinity stress. When salinity stress becomes severe, plant metabolism may collapse, leading to death. Consequently, plants have evolved strategies to regulate the salinity of the sap they transport internally.

Notably, some species, such as mangroves, thrive in coastal environments where salinity levels would be lethal to most plants by developing microscopic filtration systems that exclude excess ions. In mangrove roots, barriers such as suberin layers and the Casparian strip restrict the influx of excess

ions and water.[122] These barriers regulate ion exchange primarily through their hydrophobic surface properties. This lignin-rich, waxy layer effectively blocks the passive apoplastic water infiltration, forcing water and dissolved solutes to detour through the cytoplasm of specialized transport cells, where ion uptake can be selectively regulated. As a result, salts can enter only through controlled biological pathways. In this sense, salinity strongly influences plant survival, and the plants have evolved defense mechanisms to protect themselves from fluctuations in the salinity of the water they absorb.

Because power generation in TIH originates from electrokinetic phenomena involving interactions between charged solid surfaces and ionic species in the electrolyte, TIH devices also exhibit salinity-sensitive responses. Microscopic interactions between ions and micro/nanostructured materials, together with the associated electrokinetic effects, are widely considered to underlie this salinity dependence. In this section, we discuss how the TIH power output changes with electrolyte salinity and summarize the physical explanations currently proposed in the literature. In general, the relationship between device performance and salinity follows one of the three scenarios: (1) voltage decreases while current increases with salt concentration; (2) both voltage and current increase with salt concentration; and (3) an optimal salt concentration exists, beyond which performance declines.

7.4.1 Scenario (1): voltage is inversely proportional to the salinity. Several TIH devices operate through the streaming potential mechanism, which predicts a decrease in voltage with increasing salinity, as discussed in Section 4.1(b). This prediction has been experimentally confirmed in multiple studies.[20,74,86,94,102] For example, Li *et al.* reported salinity-dependent behavior consistent with the electrokinetic streaming mechanism using a device composed of a PAN/Al_2O_3 composite and carbon electrodes (Fig. 10a). In deionized water,

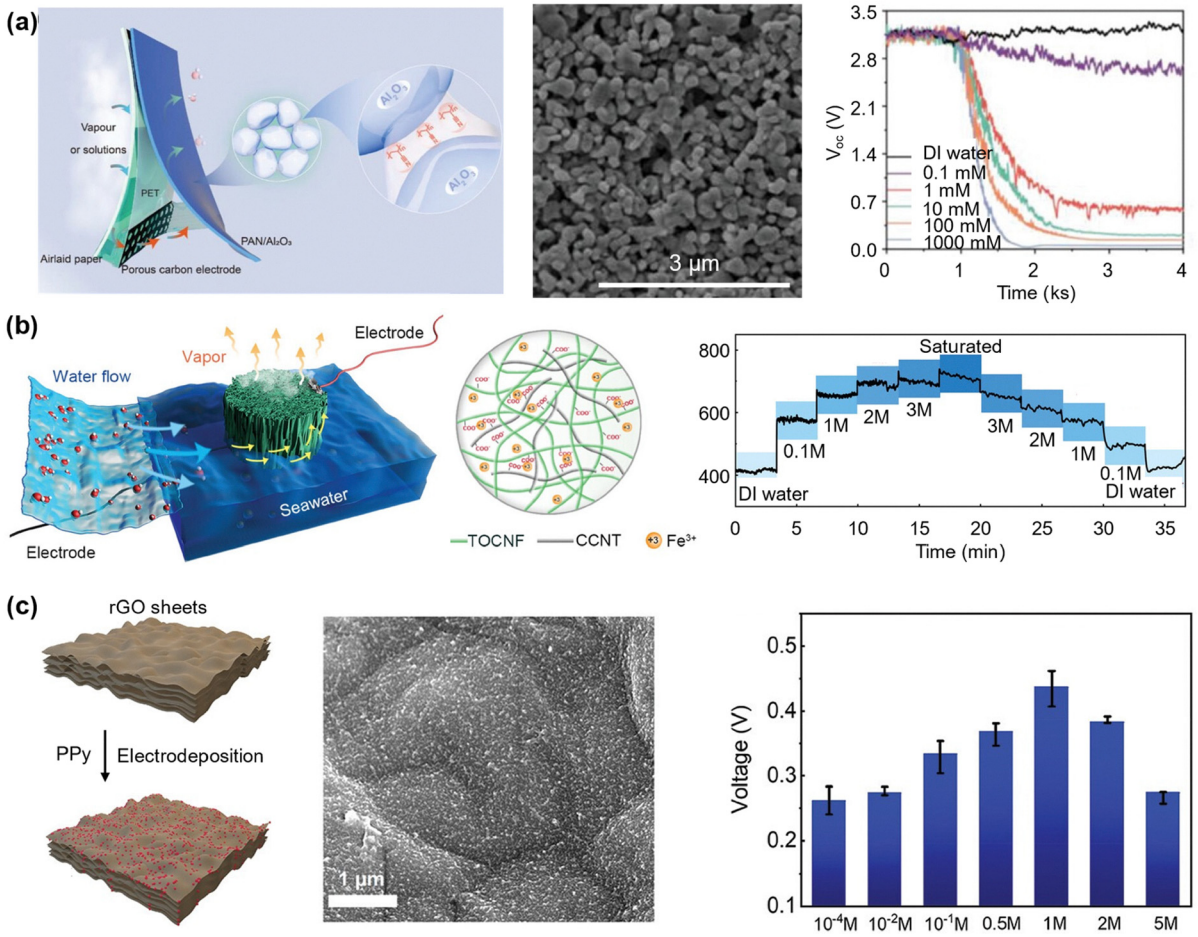

Fig. 10 Effect of salinity on voltage output in a TIH device. (a) Voltage decreases with increasing salinity in a PAN/Al_2O_3 nanoparticle composite TIH device. Left: Schematic illustration of the device. Middle: SEM image of the AN/Al_2O_3 film deposited on the device. Right: Voltage output at different electrolyte salinities. Reproduced with permission.[102] Copyright 2023, Wiley VCH. (b) Voltage profile of a TIH device made of a nanocellulose-based aerogel. Left: Schematic illustration of the working mechanism and crosslinked structure of the aerogel and CCNTs. Right: Linear response of voltage to electrolyte concentration change. Reproduced with permission.[75] Copyright 2024, Wiley VCH. (c) Optimal salinity for maximizing voltage output in an rGO/PPy composite TIH device. Left: Schematic illustration of the device fabrication process. Middle: SEM image of PPy deposited on rGO sheets. Right: Voltage profile as a function of electrolyte salinity (NaCl). Reproduced with permission.[106] Copyright 2023, Taylor & Francis.

the device generated approximately 3.0 V.[102] However, as the NaCl concentration increased from 0.1 to 1000 mM, the voltage decreased exponentially, whereas the current showed the opposite trend. The decrease in streaming potential at higher salinity was attributed to compression of the EDL, as described by the Debye–Hückel relation in eqn (17):

$$\lambda_D = \sqrt{\frac{\varepsilon\varepsilon_0 RT}{2n_{bulk}z^2F^2}} \quad (17)$$

where λ_D is the Debye length, ε, and ε_0 are the permittivities of water and vacuum, respectively; R is the ideal gas constant; T is the temperature; n_{bulk} is the bulk ion concentration; z is the ionic valence; and F is the Faraday constant. This relation indicates that increasing the electrolyte concentration (n_{bulk}) decreases the Debye length, thereby compressing the EDL. According to Li *et al.*, the densely packed PAN/Al_2O_3 particles are separated by gaps on the order of tens of nanometers. Under deionized or sufficiently dilute conditions, λ_D can approach ~100 nm, allowing EDLs on neighboring particle surfaces to overlap. Such overlap promotes ion-selective transport through the channel, amplifying the ionic imbalance generated by pressure-driven flow and resulting in high voltage output. As the electrolyte concentration increases, however, the EDL shrinks to only a few nanometers, weakening ion selectivity and reducing the generated voltage. On the other hand, the larger number of charge carriers at higher salinity increases ionic conduction and thus the streaming current.

7.4.2 Scenario (2): voltage is proportional to the salinity. In contrast to the systems described above, some TIH devices exhibit enhanced voltage output at higher salinity.[70,75,76,123] For example, Cao *et al.* synthesized a nanocellulose-based aerogel composite coated with the carboxylated carbon nanotubes (CCNTs) and containing vertically aligned water transport channels (Fig. 10b). While the device generates ~400 mV in DI water, increasing the NaCl concentration up to the near saturation point produced a monotonic increase in voltage. The authors attributed this trend to a significant increase in surface charge density on the channel walls. Several studies reporting similar salinity-dependent enhancement have likewise suggested that higher ionic concentrations promote adsorption of more ions onto channel surfaces, thereby increasing capacitive voltage generation (V_{EDL}), as discussed in Section 4.1(c) and eqn (12). At the same time, these studies also acknowledge the streaming potential mechanism, which would predict lower voltage at higher salt concentration. This apparent contradiction suggests that the interplay between salinity-dependent surface charging and electrokinetic transport remains insufficiently understood. In particular, the extent to which enhanced surface charge density can offset EDL compression requires more rigorous theoretical and experimental examination.

7.4.3 Scenario (3): optimal salinity for maximum power output. Other studies have reported the existence of an optimal electrolyte salinity that maximizes TIH power generation, which has been attributed to a tradeoff between enhanced surface charge density and physical clogging of the channel by salt crystallization during evaporation.[92,106,124–126] For example, Tian *et al.* observed this behavior in an rGO/polypyrole (PPy) composite device by varying the NaCl concentration from 0.1 mM to 5 M (Fig. 10c). The voltage increased to ~0.45 V at 1 M NaCl and then declined at higher concentrations. The authors proposed that the initial voltage increase arose from greater ion adsorption onto the rGO/PPy surface, which increased surface charge density. At higher salinity, however, rapid evaporation caused the electrolyte to reach saturation more quickly, leading to salt precipitation within the pores. These precipitated salts partially blocked the transport channels, reducing the overall evaporation rate and offsetting the benefit of increased surface charge. Although this explanation is intuitively plausible, the quantitative relationship among salinity, evaporation kinetics, crystallization, and electrokinetic output remains insufficiently resolved.

7.4.4 Challenges in elucidating salinity dependence. As discussed above, the salinity dependence of TIH power output varies substantially across systems. However, a unified theoretical framework capable of explaining these different trends is still lacking. For example, although some devices follow predictions from the classical streaming potential mechanism, it remains unclear why these systems do not also benefit from the higher surface charge density that may arise at elevated ionic strength. Conversely, in systems that perform better at high salinity, the conditions that ultimately limit output remain poorly defined. Some devices show nearly linear performance increases up to saturation, whereas others deteriorate at much lower concentrations. Beyond qualitative hypotheses involving salt crystallization and evaporation kinetics, a more quantitative physicochemical understanding is needed. From a biological perspective, trees have evolved strategies to tolerate diverse combinations of water availability and salinity. Analogously, TIH materials may benefit from microscopic engineering approaches that enable efficient ionic transport under saline conditions. For example, incorporating ion-selective membranes or root-inspired barriers that mimic suberin-rich transport regulation may provide a route toward devices that maintain performance across a wider salinity range.

7.5 Environmentally robust architectures for persistent, stable TIH power generation

The strong TIH environmental sensitivity described above can limit practical deployment, as temperature, humidity, and wind vary with weather, location, and season. To address this challenge, Yuan *et al.* reported a sealed HV system designed to produce stable voltage output while isolating the device from ambient fluctuations (Fig. 11a).[108] In their design, carbon soot deposited on glass served as the active material and CNTs served as electrodes. The device was enclosed in a transparent cylindrical container. To prevent full saturation of the carbon film in the sealed environment, the authors introduced a highly hydrophilic paper layer that redistributed water and maintained a persistent moisture gradient between the submerged bottom region and the drier upper region. This carbon–paper bilayer functioned as a passive capillary pump. The authors proposed that the bilayer enabled a self-sustaining internal

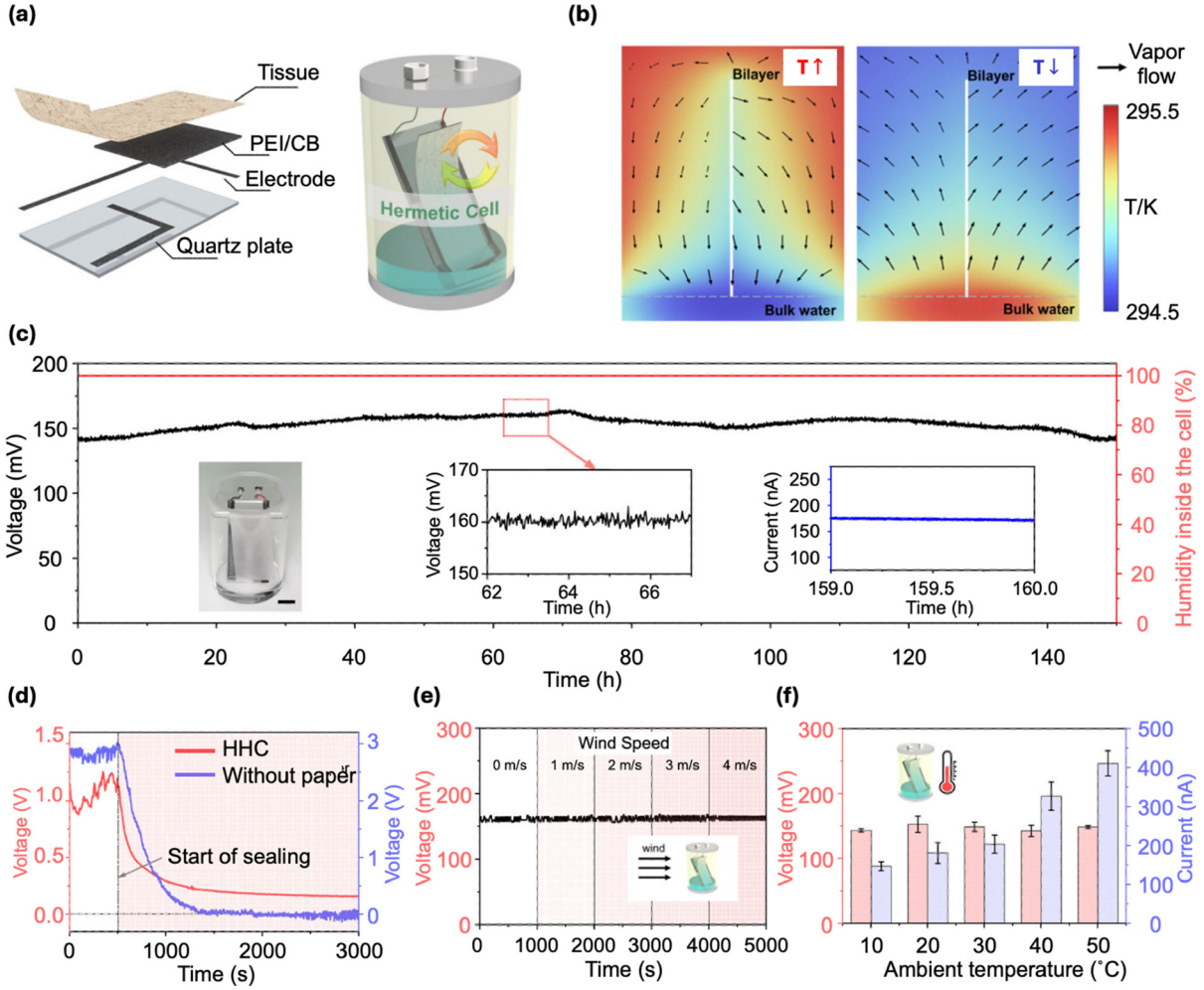

Fig. 11 Self-circulating, sealed architectures for environment-insensitive power generation. (a) Hermetic-cell concept with internal liquid–vapor circulation supported by a hydrophilic tissue layer. (b) COMSOL simulations of temperature distribution and vapor flow under high- and low-ambient-temperature conditions, showing sustained internal circulation driven by an internal temperature gradient. (c) Long-term voltage/current stability in the sealed cell at internal RH ≈ 100%. (d) Comparison with and without the tissue layer: the tissue maintains output after sealing, whereas output collapses without it. (e) Voltage invariance with external wind speed. (f) Voltage stability and increasing current with increasing temperature. Reproduced with permission.[108] Copyright 2024, Springer Nature.

water cycle driven by minute temperature differences (reported below 1 K) (Fig. 11b), producing internal transpiration and vapor convection that maintained operation for more than five days (Fig. 11c). Under sealed conditions, devices without the hydrophilic paper layer lost output, whereas the bilayer devices maintained voltage, underscoring the role of engineered water redistribution in sustaining the necessary spatial hydration gradients (Fig. 11d). Airflow had little effect on voltage in the sealed configuration, consistent with isolation from external convection (Fig. 11e), and internal humidity remained near saturation, further decoupling the system from ambient RH fluctuations. When the system temperature increased from 10 °C to 50 °C, open-circuit voltage remained nearly constant while the short-circuit current increased (Fig. 11f). The authors attributed the stable voltage to the persistence of the moisture gradient maintained by the highly hydrophilic paper layer, while the increased current was attributed to enhanced evaporation–condensation cycling and higher ion mobility at elevated temperature.

Overall, temperature, humidity, airflow, and salinity can substantially reshape TIH output because they directly regulate evaporation, capillary replenishment, and the persistence of interfacial gradients. Achieving reliable power generation therefore requires either (1) operating-condition-aware design, where geometry and deployment orientation are optimized for the local environment, or (2) self-regulating architectures, including sealed or semi-sealed systems, that maintain controlled internal water cycling and moisture gradients.

8. Substrate electrical conductivity and TIH device performance

As discussed in Section 4, classical streaming-potential theory is formulated for electrically insulating (dielectric) channels and typically requires faradaic reactions at the electrodes to continuously convert an ionic streaming current into an

electronic current. In contrast, pseudo-streaming and related ''conductive channel'' models replace the dielectric capillary wall with an electronically conductive substrate. In this setting, the solid provides an internal electronic pathway that can couple to ion motion in the liquid, allowing sustained current without relying on deliberate redox couples at the electrodes. Consequently, introducing and tuning electrical conductivity is a common design strategy in TIH devices, and varying conductive loading (or adding conductive additives) provides a straightforward knob for increasing output current.

A recurring observation, however, is that electrical conductivity introduces a trade-off between open-circuit voltage and short-circuit current.[21,26,50,109] Increasing conductivity generally increases current by reducing internal resistance, but can decrease voltage by enabling greater internal charge leakage and shunt pathways. Conversely, lower conductivity can preserve a larger voltage but limits current delivery to an external load. Many reports therefore point to an optimal conductivity, especially in composite systems, where the best performance emerges from balancing electronic conduction, capillary transport, and interfacial electrokinetic strength rather than maximizing conductivity alone.[69,70,72,76,78,93,100,104,107,126,127] In this section, we summarize representative experiments and models that clarify how conductivity controls voltage, current, and overall power output.

8.1 Voltage increases with resistivity, whereas current increases with conductivity

In Youm *et al.*'s study (Fig. 12a), conductivity was tuned by changing the carbon black loading in the deposited network. As the suspension was diluted, the device resistance increased from $\sim$1 kΩ to $\sim$18 kΩ.[26] When a droplet of 3.3 M $CaCl_2$ was introduced near the device edge, the peak voltage increased with resistance, whereas the current increased with conductivity. This behavior aligns with a simple internal-resistance picture: higher conductivity facilitates charge transport through the percolated network and therefore supports larger current, while higher resistivity suppresses internal leakage and can allow a larger potential difference to be sustained under open-circuit conditions.

8.2 Circuit models link conductivity to TIH output through shunt pathways

A closely related trend was reported by Yun *et al.* (Fig. 12b).[21] using a cotton fabric coated with conductive carbon black nanoparticles. In this system, conductivity was controlled by repeated dip-coating to create multilayer carbon networks. The authors proposed an equivalent-circuit model to rationalize why increasing conductivity can reduce voltage. Their physical picture was that cotton's intrinsic wicking concentrates water near the cotton side, so the carbon layer adjacent to the cotton becomes wetted and develops a strong EDL, whereas the outer carbon layers remain comparatively dry and contribute primarily to electronic shunting rather than interfacial charge separation. In this framework, increasing conductive loading preferentially strengthens shunt pathways and dissipates the open-circuit voltage. Using this circuit representation, the authors derived the following relations:

$$V_{OC} = V_{EDL}\left(1 - \frac{R_{wi}}{R_{wi} + R_{we}}\right) \quad (18)$$

$$I_{sc} = \frac{V_{EDL}}{R_{wi} + R_d\left(1 + \frac{R_{wi}}{R_{we}}\right)} \quad (19)$$

where R_{wi} is the resistance of the inner (wet) carbon layer, R_{we} is the resistance of the outer (dry) carbon layer, and R_d represents resistance associated with the dry portion of the coated region. Increasing the carbon loading decreases R_{we} as the exterior carbon network becomes more percolated. Eqn (18) therefore predicts a reduction in V_{OC} as R_{we} decreases, while eqn (19) predicts increased I_{SC} as the effective internal resistance drops.

This work is notable because it provided an explicit, testable framework that connects microstructural conduction pathways to macroscopic voltage–current trade-offs. A limitation is that the assumed spatial separation between ''wet, EDL-active'' and ''dry, shunting'' regions is difficult to verify directly. Spatially resolved measurements of hydration, potential, and ionic composition across thickness would strengthen the mechanistic basis and help generalize the model.

8.3 In composites, conductivity–output relationships are often nonmonotonic

In composite TIH systems, voltage and current frequently become nonmonotonic functions of substrate conductivity. This behavior reflects additional parameter couplings, including percolation thresholds, changes in surface chemistry and zeta potential, and the redistribution of water within the porous matrix. In these cases, conductivity is not an independent variable: increasing the conductive content can simultaneously change hydrophilicity, pore connectivity, and interfacial charge regulation.

Park *et al.* illustrated this complexity using a porous PDMS sponge incorporating carbon black and carbon nanotubes (CNTs) as conductive fillers (Fig. 12c).[76] A slurry of PDMS with conductive additives was infiltrated into a sugar-powder template; after curing, the sugar was dissolved to yield an interconnected porous sponge. Because PDMS is intrinsically hydrophobic, the surface was plasma-treated to enable capillary pumping. The authors varied both the total filler content (1.0–2.5 wt%) and the filler composition (carbon black, CNTs, and 1 : 1 mixtures). As expected, conductivity increased with filler loading, and CNT-containing samples percolated more efficiently due to CNTs' higher aspect ratio. Electrical output, however, did not track conductivity monotonically. Beyond a threshold filler content, slurry viscosity increased and infiltration into the sugar template became nonuniform, producing defects that blocked solution transport and degraded performance. Moreover, the sample with the highest conductivity (pure CNTs) produced the lowest voltage, consistent with enhanced internal shunting. Notably, the highest voltage occurred at an intermediate composition (2 wt% CB/CNT mixture), whereas the most resistive sample (pure CB) did not yield the highest

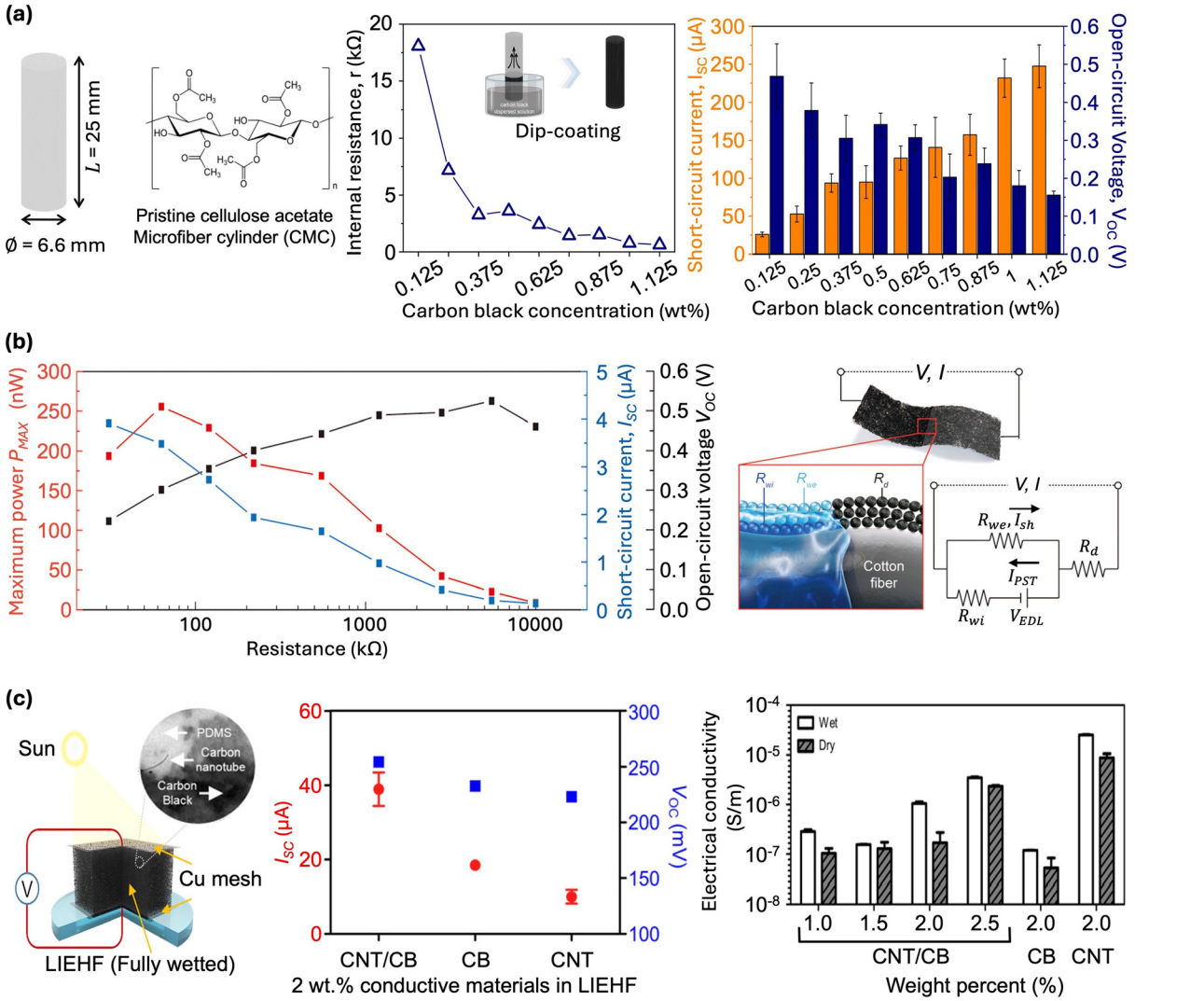

Fig. 12 Output dependence on electronic conductivity in TIH devices. (a) Cellulose acetate microfiber cylinder (CMCG): device schematic, geometry, and molecular structure. Internal resistance decreases with increasing carbon-black loading (controlled *via* dip-coating from suspensions of different concentration; inset). Voltage and current exhibit opposite trends with carbon-black weight fraction. Reproduced with permission.[26] Copyright 2023, Elsevier. (b) Cotton fabric coated with carbon black: maximum power, current, and voltage *versus* internal resistance, with an equivalent-circuit model illustrating how conductive "shunt" pathways reduce V_{OC} while increasing I_{SC}. Reproduced with permission.[21] Copyright 2019, American Chemical Society. (c) Porous PDMS sponge with carbon black (CB) and CNT fillers: device concept (left), voltage/current output (middle), and conductivity *versus* CB/CNT composition (right). Reproduced with permission.[76] Copyright 2021, American Chemical Society.

voltage either. The authors attributed the optimum to interfacial electrokinetics rather than conductivity alone: the intermediate mixed-filler sample exhibited the largest measured zeta potential, consistent with stronger counterion attraction and enhanced EDL-mediated selectivity. They also emphasized that excessive conductive loading can obstruct capillary pathways, reduce water infiltration, and weaken EDL formation, which can outweigh gains from lower electronic resistance.

Across these studies, electrical conductivity is a key determinant of current generation, but it does not uniquely determine TIH voltage output. Increasing conductivity can increase I_{SC} while decreasing V_{OC} through internal leakage and shunt pathways. In composite systems, conductive additives also perturb pore structure, wetting, and surface charge regulation, producing nonmonotonic behavior and shifting the optimal loading. These results reinforce a practical design principle: in TIH, voltage is set primarily by interfacial electrokinetic strength (EDL formation, charge regulation, and ion selectivity), whereas conductivity governs how efficiently that electric motive force is converted into usable current. Optimizing TIH performance therefore requires co-optimizing conductivity with capillary transport and interfacial chemistry, rather than tuning conductivity in isolation.

9. Applications of TIH harvesters

With the rapid advancement in TIH device development, attention has increasingly shifted from proof-of-concept

demonstrations toward practical applications. Because TIH output can be amplified through modular integration of multiple units in series and parallel, recent studies have moved beyond powering light-emitting diodes and small electronic components to demonstrate operation of electrochemical reactors,[94,96,97] and ionic[67,69,74,102,112] and chemical sensors.[128,129] In this section, we highlight representative examples that illustrate how TIH output can be translated into useful functions and discuss the constraints that currently limit broader deployment.

9.1 TIH-powered decentralized electrochemical processes and resource recovery

One of the most promising application spaces for TIH is decentralized electrochemical operation. Early demonstrations showing TIH devices powering LEDs and small electronics established that evaporation-driven electricity can be harvested continuously under ambient conditions. More recent work has extended this concept to electrochemical systems, which require sustained electrical input to drive charge transfer reactions. These include water electrolysis, dialysis, and redox-based chemical conversions, and potentially critical mineral recovery.

9.1.1 TIH-powered water electrolysis. In 2024, Jeong and co-workers demonstrated TIH-driven water splitting using commercial cosmetic removal pads coated with carbon black nanoparticles (Fig. 13a).[97] Delivering $CaCl_2$ solution to one edge of each unit produced an electrical output that was scaled by series/parallel integration. The assembled array powered an electrolyser using a PCo/NF cathode for the hydrogen evolution reaction (HER) and a Co_3O_4/NiFe-LDH/NF anode for the oxygen evolution reaction (OER). By combining multiple units, the system achieved an open-circuit voltage of 2.09 V and a short-circuit current of 3.11 mA, exceeding the practical threshold required for alkaline water splitting. The device produced approximately 80 μmol of H_2 over 1 hour. Although this demonstration required more than 30 individual TIH units, it highlights an important practical feature of the technology: output can be scaled through simple modular integration rather than by fabricating a single large monolith. More broadly, this result points to an opportunity for TIH in off-grid electrochemical processing, where distributed, low-cost generators could be coupled directly to catalytic electrodes, membranes, or microreactors.

9.1.2 Coupled mineral recovery and energy harvesting. Beyond powering electrochemical reactions, TIH architectures may also be integrated with resource-recovery functions.

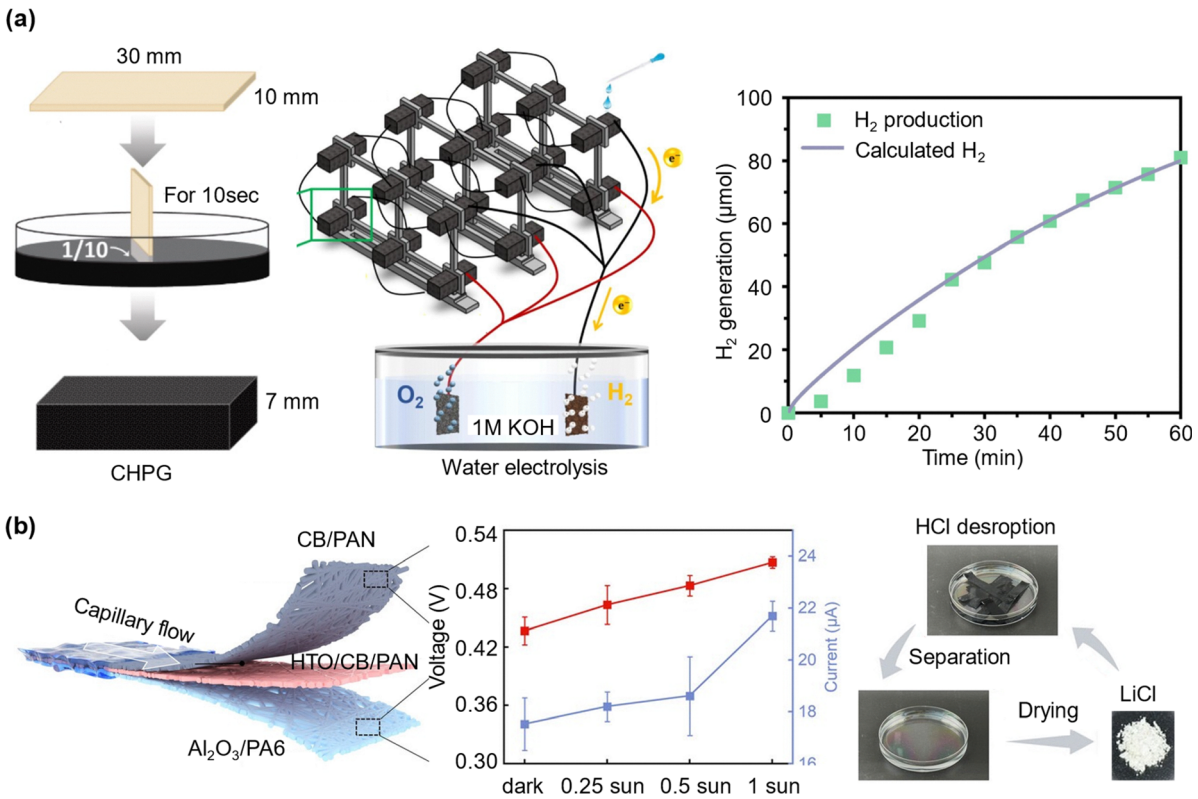

Fig. 13 Representative and emerging applications of TIH devices in resource recovery. (a) TIH-powered water electrolysis and hydrogen generation. Right: Fabrication schematic of a cellulose-sponge-based hydrovoltaic power generator (CHPG) and the electrolysis setup enabled by series/parallel CHPG arrays. Reproduced with permission.[97] Copyright 2024, Elsevier. (b) Integrated TIH power generation and lithium harvesting. Left: Schematic of a device consisting of a CB/PAN layer (for TIH power generation), a HTO/CB/PAN layer (for lithium adsorption), and an Al_2O_3 substrate. Middle: Power output as a function of sun light intensity. Right: Lithium salt recovery process. After operation, the devices are immersed in HCl solution and then dried to obtain LiCl salt; the devices can be reused for both electricity generation and lithium harvesting. Reproduced with permission.[130] Copyright 2025, Wiley VCH.

The growing demand for critical minerals such as lithium has intensified interest in extraction technologies with lower chemical and environmental footprints than conventional mining and refining.[131] In this context, Lin *et al.* reported a combined TIH device and evaporation-driven lithium harvesting system (Fig. 13b).[130] The device consists of an Al_2O_3 substrate, a PAN fiber coated with protonated lithium titanate (HTO) and CB for lithium adsorption, and a PAN/CB layer for TIH power generation. Brine infiltrates the upper PAN-based layers, where Li^+ is selectively adsorbed by the HTO-containing layer, while capillary flow, enhanced by solar-thermal evaporation, drives water transport. Simultaneously, the upper PAN/CB layer generates electricity through the TIH mechanism. Under 1-sun illumination, the device produced 0.48 V and ~22 μA. After the operation, adsorbed lithium was recovered by immersing the device in HCl solution to induce desorption, followed by drying to yield LiCl powder.

This study highlights the possibility of using transpiration-inspired architectures to merge sustainable energy harvesting and mineral recovery within a single platform. However, the electricity generated by the TIH component was not yet actively used to drive an additional electrochemical extraction step. This is an important direction for future work. For example, electrochemical lithium extraction based on battery-type electrode materials has previously been proposed for seawater and brine systems.[132] If the electrical energy required for such charge/discharge-assisted separations could be supplied locally by TIH devices, it would create a more tightly integrated nexus between water transport, energy harvesting, and critical mineral recovery.

9.2 TIH-powered distributed chemical sensing and environmental monitoring

In addition to acting as a power source, TIH devices can function as transducers because their electrical output is intrinsically sensitive to interfacial charge, ion transport, and environmental conditions. This feature makes TIH especially attractive for sensing applications, where the target analyte or surrounding environment modulates the same physicochemical processes responsible for electricity generation.

9.2.1 Self-powered chemical sensing. A direct example is chemical sensing based on analyte-induced changes in surface charge and electrokinetic transport. Zhou *et al.* developed a self-powered sensor for Congo red (CR) using a composite membrane of polyacrylonitrile (PAN) and a covalent organic framework (COF), TpPa (Fig. 14a).[128] TpPa exhibits a strongly negative zeta potential (reported as −51.3 mV), which supports robust EDL formation and voltage generation. Because TaPa adsorbs CR, analyte binding alters the effective surface charge and reduces the zeta potential of the membrane. As CR loading increases, the device voltage decreases accordingly, enabling quantitative detection. Using this mechanism, the sensor detected CR concentrations from 1 to 33 ppm, demonstrating that TIH output can serve directly as a sensing signal without an external power supply.

9.2.2. Environmental monitoring and smart packaging. TIH devices are also highly sensitive to ambient variables such as humidity and temperature, as discussed in Section 7.[134] This environmental responsiveness suggests their utility as self-powered monitoring platforms. To move beyond simply observing output variation, however, TIH systems must be integrated with application-specific architectures that convert environmental changes into actionable information. An example was reported by Liu *et al.*, who incorporated a TIH-based device into agricultural packaging to monitor product damage through humidity changes arising from juice leakage (Fig. 14b).[133]

The device was fabricated on a flexible substrate by screen printing activated carbon (AC) and graphene oxide (GO)/AC composite inks to form functional micro/nanochannels. AC was also printed as the electrode material, after which a poly(vinyl alcohol) (PVA) gel electrolyte containing LiCl was deposited and dried. When humidity increases, water vapor is absorbed by the PVA gel, facilitating Li^+ transport across the device and generating a voltage. Ion diffusion through the GO/AC channel sustains TIH-associated output. This mechanism enables practical damage indication in packaged agricultural products. When fruit or other produce is damaged, leaked juice increases the humidity inside the package, which activates the device and powers a red LED array to provide a clear visual warning. Such systems illustrate how TIH can be embedded into low-cost, disposable packaging for distributed quality control without requiring batteries or external electronics.

9.3. Flexible and wearable TIH systems for real-time physiological monitoring

Wearable and epidermal electronics motivate self-powered platforms that can operate from physiological fluids. Sweat contains ions such as Na^+, K^+, and Ca^{2+}, providing a naturally replenished electrolyte source during exercise or daily activity. Despite the promise of wearable sensors for real-time health monitoring, one of their persistent limitations is dependence on external power supplies, which often increase device weight, stiffness, and complexity.

Because TIH systems have already demonstrated electricity generation from ionic aqueous electrolytes, we therefore reason that they must be well suited for sweat-powered wearable platforms. Indeed, several groups have explored TIH-like devices integrated into textiles or flexible substrates.[135] Luo *et al.* deposited carbon black and chemically oxidized multiwalled carbon nanotubes (MWCNTs) onto discarded mask straps and demonstrated electricity generation in several electrolytes, including NaCl, KCl, and LiCl solutions.[112] In LiCl, the device generated >0.7 V and ~60 μA. The authors then integrated the device into clothing and tested it during vigorous exercise. As sweat was absorbed into the fibrous substrate, the device produced >0.4 V and continued generating output until the substrate dried during the subsequent rest period (Fig. 14c). The signal persisted for nearly 1 hour, demonstrating that perspiration can sustain a continuous measurable signal in a wearable form factor. While this study did not yet close the loop by powering a specific on-body electronic system or performing quantitative analyte sensing, it establishes the fundamental feasibility of TIH operation in textiles and clarified the main engineering requirement: maintaining a stable wet–dry gradient or sustained evaporation pathway in a mechanically robust, wearable architecture.

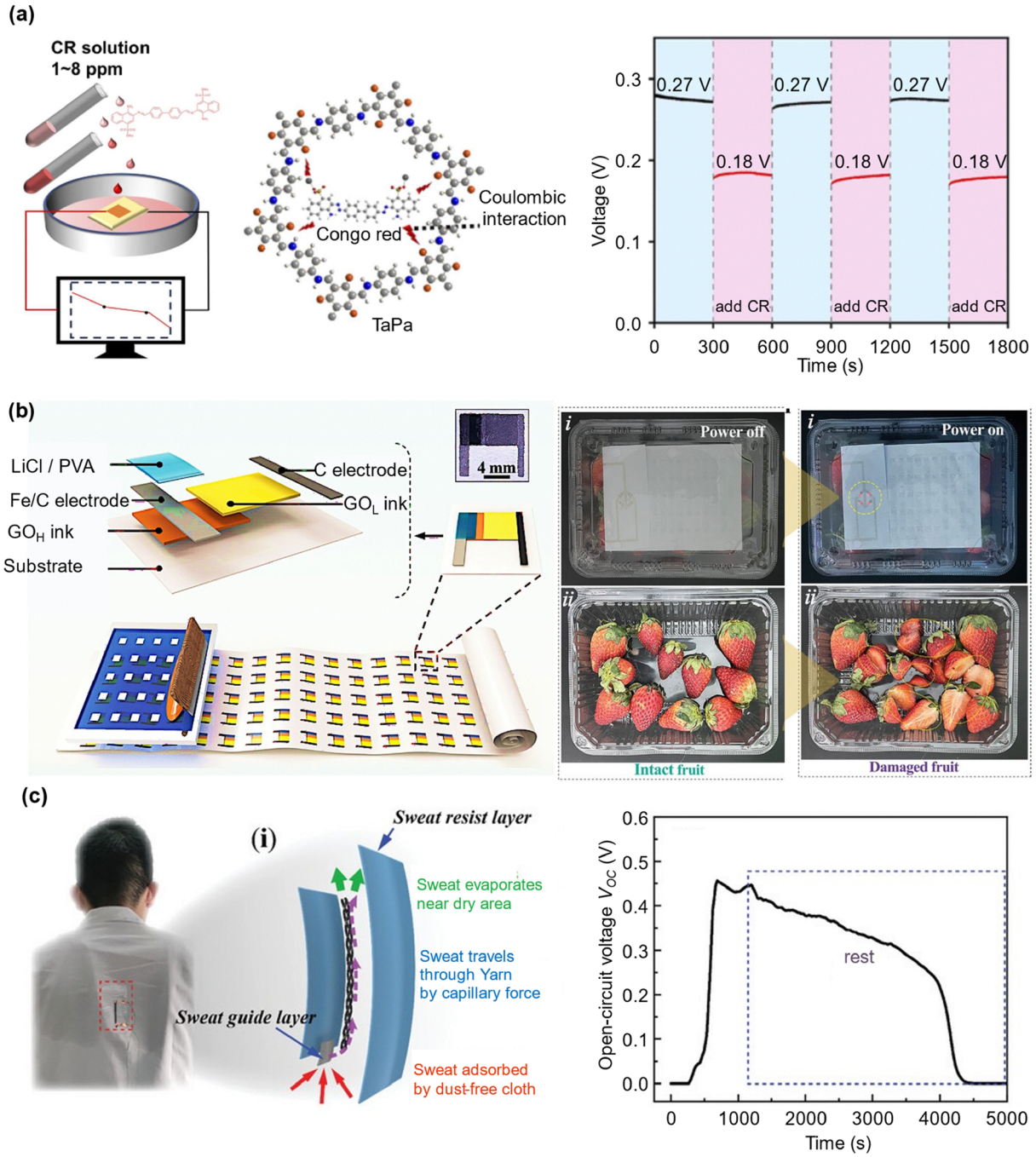

Fig. 14 Representative and emerging applications of TIH devices on self-powered sensing. (a) Self-powered chemical sensing of Congo red (CR). Left: Sensing concept. Middle: Proposed binding mechanism between the active ingredient TaPa and CR. Right: Cycling tests show voltage suppression upon CR binding. Reproduced with permission.[128] Copyright 2025, Elsevier. (b) Flexible and scalable TIH device for agricultural product quality monitoring. Left: Schematic illustration of device components and screen-printed array on a flexible substrate. GO$_H$ denotes a GO mixture with high activated carbon (AC) content, whereas GO$_L$ denotes low AC content. Inset: Optical image of a single device unit. Right: Device powered by the humidity increase caused by juice leaking from damaged fruit inside the package. Reproduced with permission.[133] Copyright 2024, Wiley VCH. (c) Wearable TIH device for sweat sensing, integrated into a fibrous strap and operated while attached to clothing. Green arrows indicate evaporation-driven liquid loss; red arrows indicate sweat inflow. Reproduced with permission.[112] Copyright 2023, Wiley VCH.

9.4. From demonstrations to deployable systems

Although TIH remains an emerging technology, these examples demonstrate a clear progression from basic proof-of-concept demonstrations toward functional systems. Electrolysis highlights the ability of TIH arrays to achieve application-relevant voltage and current through modular scaling. Integrated lithium harvesting points to multifunctional platforms that combine water transport, energy generation, and resource recovery. Chemical

sensing demonstrates that TIH can serve not only as a power source but also as a transduction mechanism, while packaging and wearable implementations illustrate how environmental or physiological inputs can be converted directly into actionable outputs. Going forward, the most consequential advances will likely arise from co-designing TIH architecture with the intended application. This includes packaging strategies that stabilize evaporation, materials engineering approaches that resist fouling in saline or biological fluids, and standardized load-matching methods that efficiently translate TIH output into usable electrical work. Progress in these areas will be essential for moving TIH from laboratory demonstrations toward practical platforms for distributed sensing, flexible electronics, and decentralized electrochemical technologies.

10. Challenges and outlook

Transpiration-inspired hydrovoltaics (TIH) has advanced rapidly from early proof-of-concept demonstrations to devices that can sustain voltage output under ambient conditions and, through modular integration, power practical loads ranging from sensors to electrochemical reactions. At the same time, the field remains mechanistically and technologically immature. The central bottleneck is not simply achieving higher output, but establishing predictive theoretical frameworks that connect evaporation-driven water transport, evolving hydration states, and interfacial electrokinetics to measurable voltage, current, and power under load. In this section, we summarize key challenges and outline research opportunities that could transform TIH from an intriguing phenomenon into a designable and deployable energy-harvesting platform.

10.1 Plant hydraulics as a blueprint for TIH design

TIH has a distinctive advantage among emerging energy-harvesting concepts because the natural process it emulates, evaporation-driven water transport in plants, has been studied quantitatively for decades. Progress in TIH could be accelerated by treating these devices not simply as isolated porous films, but as engineered analogs of the soil-root-xylem-leaf continuum, and by translating established plant-hydraulics principles into device-level design rules.

Root-inspired intake. Real deployment environments rarely provide an ideal, well-mixed water reservoir. Instead, water arrives intermittently, heterogeneously, and often in the presence of salts, particulates, or foulants. Root systems address this challenge through distributed uptake, moisture-seeking growth, and local buffering. TIH devices can borrow these principles through branched wicking networks that expand the capture area, graded wettability that preferentially draws water from wetter regions, and inlet layers that reduce salinity or fouling before water reaches the active transduction region.

Xylem-inspired transport. Xylem balances high hydraulic conductance with resistance to cavitation through anisotropy, hierarchy, and compartmentalization. Comparable TIH architectures may include vertically aligned conduits for directional flow, hierarchical pore networks that combine rapid transport in larger pores with ion selectivity in smaller pores, and pit-like constrictions that suppress runaway drying and limit air invasion.

Leaf-inspired evaporation control. Leaves maximize evaporative area while tightly regulating water loss through microstructure, surface chemistry, and boundary-layer effects. TIH can emulate this using passive, high-area evaporative interfaces that sustain a stable saturation gradient without drying the transport backbone, thereby improving both output and stability without reliance on external heating.

Adopting plant-hydraulic metrics such as hydraulic conductance, saturation profile, capillary pressure, and failure threshold under evaporative demand could provide a common quantitative language linking water transport to electrokinetic output. This roots-xylem-leaf framework shifts scaling away from merely enlarging device area and toward co-designing intake, transport, and evaporation modules for robust and high-output operation.

10.2 Treating evaporation as a quantitative driver rather than a qualitative prerequisite

Most mechanistic descriptions of TIH emphasize electrokinetic processes associated with EDL formation and selective ion transport, while treating evaporation primarily as a boundary condition that ''maintains flow.'' Yet almost all experimental studies identify evaporation as essential, and several report that it amplifies output beyond what classical electrokinetic streaming predicts. In plants, evaporation is not merely permissive. It generates a sustained water-potential gradient and can induce MPa-scale tension that stabilizes long-range flow. Translating this insight to TIH requires models that incorporate evaporation explicitly and quantitatively.

A central gap is the lack of constitutive links between (1) evaporation flux at the device surface, (2) the resulting pressure distribution and saturation profile within the porous network, and (3) the electrokinetic source terms that generate voltage and current. Progress will likely require coupling porous-media transport (for example, Darcy flow with unsaturated permeability and capillary pressure–saturation relations) to ion transport and charge regulation (for example, Poisson–Nernst–Planck with surface charge that depends on pH and ionic strength), and then embedding these physics into an equivalent circuit or energy-balance framework that predicts measurable output under load. Establishing scaling laws that relate power density to measurable parameters such as evaporation rate, effective permeability, zeta potential, conductivity, and device hydration length would immediately enable rational design and fair comparisons across studies.

10.3 Identifying optimal channel architectures through controlled structure–function comparisons

A wide range of channel conformations has been reported, including vertically aligned vascular templates, layered 2D nanochannels, honeycomb networks, random nanoporous

packings, and hierarchical micro–nano structures. Each architecture can be argued to ''improve'' TIH performance, but the literature still lacks controlled comparisons that isolate geometry from chemistry and composition. As a result, it remains unclear which structural motif is optimal for a given goal: maximizing peak power density, maximizing stability under salinity, minimizing sensitivity to humidity, or sustaining operation under intermittent wetting.

The path forward is to build structure–function maps under matched material chemistry. For example, families of architectures made from the same base material (or with standardized surface functionalization) could be compared while measuring hydraulic conductance, evaporation flux, saturation gradients, pore-size distributions, and effective ionic selectivity. Importantly, performance metrics should extend beyond open-circuit voltage and short-circuit current to include maximum power point under load, energy delivered per unit water evaporated, and lifetime under repeated cycling. Such datasets would reveal whether the best designs are those that maximize interfacial area, those that maximize directional conductance, or those that best stabilize a spatially persistent wet–dry asymmetry, and how these priorities shift with salinity and environment.

10.4 Distinguishing true hydrovoltaic output from electrochemical artifacts

One of the persistent sources of confusion in the hydrovoltaic field is the role of electrochemical reactions at the electrode–electrolyte interface. To clarify TIH as a distinct mechanism of power generation, it is essential to distinguish the redox reactions that are inherently required to convert ionic current into electronic current from additional electrochemical processes that effectively turn the system into a primary battery. As discussed in Section 4, classical streaming-potential systems inevitably involve electrode reactions that complete the circuit and enable charge transfer. At the same time, some studies intentionally introduce electrochemically active electrodes or redox-coupled electrolytes, for example, by using reactive metals in saline solutions, to enhance output. Although such synergistic coupling may be useful for boosting practical performance, the distinction between intrinsic redox processes required for current conversion and parasitic or deliberately added battery-like chemistry must be stated explicitly.

Even when studies employ carbon-based or nominally inert electrodes and provide supporting characterization, such as cyclic voltammetry or impedance spectroscopy, complete exclusion of electrochemical contributions remains difficult. This is especially true when electrodes contact electrolyte solutions under evaporation, where concentration gradients, dissolved oxygen gradients, and local pH shifts can develop over time. Because even small parasitic faradaic currents can distort voltage-current behavior, rigorous controls are essential, particularly in studies claiming long-term stability, unusually high voltage, or operation in complex electrolytes.

Stronger separation will likely require experimental protocols designed explicitly to falsify electrochemical explanations. Examples include: symmetric-electrode controls that suppress galvanic potentials, reference-electrode measurements to track local electrode potentials, electrolyte replacement experiments that hold conductivity constant while changing redox chemistry, and electrode-sealed devices that eliminate faradaic redox processes (for non-traditional streaming potential TIH systems). Spatially resolved measurements of ionic concentration and pH along the device could also clarify whether output is linked to bulk gradients (which may drive electrochemical potentials) or to interfacial electrokinetic coupling in the porous network. Establishing ''electrochemistry-free'' benchmarks would strengthen the credibility of TIH as a distinct energy-harvesting modality and improve comparability across materials and designs.

10.5 Evaluating practicality through scaling and application-relevant metrics

Most TIH demonstrations remain at the laboratory scale, often powering LEDs or intermittent low-power electronics. Moving toward practical deployment requires advances along two parallel routes: increasing power density of a single unit and scaling output through manufacturable arrays. Both routes depend on packaging and systems engineering, not only on materials.

First, device packaging must stabilize the evaporation boundary condition and protect performance against fluctuations in humidity, wind, fouling, and mechanical disturbance. Semi-sealed architectures that maintain an internal water cycle, engineered ''leaf'' surfaces that maximize evaporation area without triggering premature drying, and antifouling designs for saline or biofluid environments will be essential for reliable operation. Second, scaling should be evaluated using application-relevant metrics: power delivered at the maximum power point, energy per unit evaporated water, volumetric and areal power density, cycling lifetime, and cost per watt for scalable fabrication. Third, integration with power management electronics (rectification, regulation, and storage) and with specific loads (sensors, transmitters, and electrochemical cells) will be required to translate TIH outputs into robust system-level function. Without these system-level considerations, improvements in open-circuit voltage or short-circuit current alone are unlikely to translate into practical utility.

10.6 Expanding material design through functionalization and interfacial engineering

A broadly accepted design principle in TIH is that high-performing materials should combine hydrophilicity with high surface charge, thereby promoting water transport, electric double-layer formation, and ionic current generation. Accordingly, widely studied materials such as carbon black, carbon nanotubes, graphene oxide, and metal oxides have been used extensively to exploit their favorable surface properties. Composite systems, including mixed carbon-black/CNT networks, have also been explored to combine complementary attributes.

However, systematic chemical functionalization as a deliberate strategy for optimizing TIH performance remains underdeveloped. For example, oxidation of carbon materials can introduce hydrophilic functional groups that improve wettability, increase

surface charge density, and strengthen ionic transport within the electric double layer. At the same time, oxidation can reduce intrinsic electrical conductivity, creating a tradeoff that must be optimized carefully. This suggests that TIH material design should move beyond simple material selection toward quantitative interfacial engineering that balances surface charge enhancement, wettability, pore accessibility, and electronic transport. In addition, covalent modification or crosslinking of base materials with functional molecules may provide a route to tailor interfacial properties more precisely. Such approaches could enable systematic tuning of acidity, ion affinity, antifouling behavior, and hydration stability, opening a broader materials-design space for TIH than is currently represented in the literature.

10.7 Integrating TIH with complementary systems for a synergistic effect

At present, many TIH studies emphasize either maximizing output or demonstrating that the signal changes in response to environmental stimuli. For instance, reduced output at high humidity is often cited as evidence that TIH may serve as a humidity sensor. However, most demonstrations remain at the level of passively observing output fluctuations rather than converting those fluctuations into actionable functionality. True practical value will come not from simply reading a changing signal, but from integrating TIH with complementary systems that actively communicate, regulate, or exploit that signal.

One promising direction is agricultural monitoring. As discussed in Section 6, both tree physiology and TIH device performance are strongly influenced by water availability and salinity. This analogy suggests the possibility of TIH-based platforms for monitoring soil moisture and salt stress in agricultural settings. During drought, reduced soil water content and concurrent changes in ion concentration would alter TIH output, potentially allowing localized detection of water deficiency or nutrient imbalance. Such distributed sensing could help farmers direct irrigation or fertilization more precisely, rather than applying resources uniformly across an entire field. Another opportunity lies in coupling TIH with solar desalination or water-treatment technologies. Ocean-deployed or brine-exposed TIH arrays could benefit from the abundant water supply, while solar desalination systems already rely on porous micro–nano architectures with high surface area for water transport and rapid evaporation. Because these same structural features are also favorable for TIH, integrating the two systems could create synergistic platforms for concurrent water purification and electricity generation.

More broadly, the most compelling near-term niches for TIH may be distributed, low-power settings where water is already present and evaporation is unavoidable, such as soil and infrastructure monitoring, wearable or textile-based sensing, and water-treatment interfaces. In these contexts, TIH may be most valuable not as a competitor to batteries or photovoltaics on energy density, but as a maintenance-free trickle-power source that converts an ambient water flux into persistent electrical functionality.

TIH stands at an important transition point. The field has clearly established that evaporation-driven water transport through charged porous media can generate useful electrical output, yet it has not fully matured into a predictive engineering discipline. The next phase of progress will depend on moving beyond isolated demonstrations toward quantitative frameworks, controlled benchmarking, and application-driven design. If these challenges are addressed, TIH could evolve into a distinctive class of energy-harvesting technologies that leverage ubiquitous water fluxes for persistent, low-power operation in environments where conventional power sources are impractical or undesirable.

11. Conclusion

Evaporation is involved in one of the most powerful and spatially distributed energy conversion processes on Earth, yet it has historically been harvested only after the water cycle concentrates that energy into macroscopic motion, as in rivers and hydroelectric plants. Transpiration-inspired hydrovoltaics offers a complementary route: harvesting energy closer to the source by rectifying evaporation-sustained capillary transport into electrical output within microstructured and nanostructured solids. By drawing a direct analogy to tree hydraulics, TIH devices exploit the same core ingredients that make transpiration effective, including capillary-driven water supply, persistent evaporation at exposed interfaces, and strong water–solid interactions under confinement. Across the literature, TIH systems have demonstrated that voltage and current can be sustained under ambient conditions, can be tuned through geometry, microarchitecture, conductivity, and environment, and can be scaled through modular integration to power practical functions such as sensing and electrochemical reactions. At the same time, the field faces clear mechanistic and engineering challenges. The central need is a predictive framework that couples evaporation-driven unsaturated flow to interfacial charge regulation and ion transport, enabling quantitative scaling laws and principled optimization. Controlled comparisons of channel architectures, rigorous exclusion of electrochemical artefacts, and application-relevant performance metrics will be essential for establishing TIH as a mature energy-harvesting technology. More broadly, TIH reframes evaporation from a loss mechanism into an opportunity for distributed energy conversion. If the community can unify transpiration physics with electrokinetic transduction in a quantitative, designable framework, TIH could emerge as a new paradigm for low-cost, distributed power in the water–energy nexus, enabling autonomous devices that operate where moisture and evaporation are naturally abundant.

Author contributions

ATL: conceptualization, writing – review and editing, supervision, writing – original draft and project administration.

JW: conceptualization, investigation, writing – original draft, and visualization.

Conflicts of interest

There are no conflicts to declare.

Data availability

This review article did not generate or analyze any new datasets. All data discussed are derived from previously published studies and are cited in the article and its references. Any datasets underlying the cited works are available from the corresponding original publications and, where applicable, from the repositories listed by those authors.

Acknowledgements

The authors are grateful to NSF for the award #2243104, CENTER FOR COMPLEX PARTICLE SYSTEMS (COMPASS). The work was also supported by an ACS PRF Doctoral New Investigator grant (Grant Number: 66979-DNI10). We thank the Michigan Materials Research Institute (MMRI). The authors also wish to acknowledge the support from the University of Michigan Institute of Energy Studies and the Bold Challenges Boost program.

References

1 G. L. Stephens, *et al.*, An update on Earth's energy balance in light of the latest global observations, *Nat. Geosci.*, 2012, **5**, 691–696.
2 B. R. Scanlon, *et al.*, Global water resources and the role of groundwater in a resilient water future, *Nat. Rev. Earth Environ.*, 2023, **4**, 87–101.
3 A.-H. Cavusoglu, X. Chen, P. Gentine and O. Sahin, Potential for natural evaporation as a reliable renewable energy resource, *Nat. Commun.*, 2017, **8**, 617.
4 J. Frijns, J. Hofman and M. Nederlof, The potential of (waste)water as energy carrier, *Energy Convers. Manage.*, 2013, **65**, 357–363.
5 X. Wang, *et al.*, Hydrovoltaic technology: from mechanism to applications, *Chem. Soc. Rev.*, 2022, **51**, 4902–4927.
6 A. Evans, V. Strezov and T. J. Evans, Assessment of sustainability indicators for renewable energy technologies, *Renewable Sustainable Energy Rev.*, 2009, **13**, 1082–1088.
7 Y. Li, G. Zhao, G. H. Allen and H. Gao, Diminishing storage returns of reservoir construction, *Nat. Commun.*, 2023, **14**, 3203.
8 Y. Nagata, K. Usui and M. Bonn, Molecular Mechanism of Water Evaporation, *Phys. Rev. Lett.*, 2015, **115**, 236102.
9 F. Zhao, Y. Guo, X. Zhou, W. Shi and G. Yu, Materials for solar-powered water evaporation, *Nat. Rev. Mater.*, 2020, **5**, 388–401.
10 V.-D. Dao, N. H. Vu, H.-L. Thi Dang and S. Yun, Recent advances and challenges for water evaporation-induced electricity toward applications, *Nano Energy*, 2021, **85**, 105979.
11 A. Ashrafi, *Quantum Confinement: An Ultimate Physics of Nanostructures, Encyclopedia of Semiconductor Nanotechnology*, 2011.
12 C. Hamaguchi, *Basic Semiconductor Physics*, Springer International Publishing, Cham, 2017, DOI: 10.1007/978-3-319-66860-4.
13 Y. D. Wang, Solar-driven abnormal evaporation of nanocomfined water, *Sci. Adv.*, 2012, **10**, 22.
14 X. Liu, *et al.*, Power generation from ambient humidity using protein nanowires, *Nature*, 2020, **578**, 550–554.
15 K. Liu, *et al.*, Induced Potential in Porous Carbon Films through Water Vapor Absorption, *Angew. Chem., Int. Ed.*, 2016, **55**, 8003–8007.
16 J. D. Scharwies and J. R. Dinneny, Water transport, perception, and response in plants, *J. Plant Res.*, 2019, **132**, 311–324.
17 H. R. Brown and A. P. Sutton, Trees suck. Notes on the physics of transpiration in trees, *Prog. Biophys. Mol. Biol.*, 2025, **195**, 71–86.
18 M. Ha, M. Morrow and K. Algiers, Botany, ASCCC Open Educational Resources Initiative, 2023.
19 T. D. Wheeler and A. D. Stroock, The transpiration of water at negative pressures in a synthetic tree, *Nature*, 2008, **455**, 208–212.
20 G. Xue, *et al.*, Water-evaporation-induced electricity with nanostructured carbon materials, *Nat. Nanotechnol.*, 2017, **12**, 317–321.
21 T. G. Yun, J. Bae, A. Rothschild and I.-D. Kim, Transpiration Driven Electrokinetic Power Generator, *ACS Nano*, 2019, **13**, 12703–12709.
22 S. G. Yoon, *et al.*, Natural Evaporation-Driven Ionovoltaic Electricity Generation, *ACS Appl. Electron. Mater.*, 2019, **1**, 1746–1751.
23 E. Herbert, S. Balibar and F. Caupin, Cavitation pressure in water, *Phys. Rev. E: Stat., Nonlinear, Soft Matter Phys.*, 2006, **74**, 041603.
24 A. Boatwright, S. Hughes and J. Barry, The height limit of a siphon, *Sci. Rep.*, 2015, **5**, 16790.
25 N. Lu and J. K. Mitchell, *Geotechnical Fundamentals for Addressing New World Challenges*, Springer International Publishing, Cham, 2019.
26 J. Youm, *et al.*, Highly increased hydrovoltaic power generation via surfactant optimization of carbon black solution for cellulose microfiber cylindrical generator, *Surf. Interfaces*, 2023, **38**, 102853.
27 W. L. Powers, Physical Edaphology: The Physics of Irrigated and Non-irrigated Soils: By Sterling A. Taylor, and Gaylen L. Ashcroft. W. H. Freeman and Co., 660 Market Street, San Francisco, Calif. 94104. 1972. 533 pages. 279 illus. 46 tables. $17.50, *J. Environ. Qual.*, 1974, **3**, 188.
28 S. Han, W. Kim, H. J. Lee, R. Joyce and J. Lee, Continuous and Real-Time Measurement of Plant Water Potential

Using an AAO-Based Capacitive Humidity Sensor for Irrigation Control, *ACS Appl. Electron. Mater.*, 2022, **4**, 5922–5932.
29 P. Jain, *et al.*, A minimally disruptive method for measuring water potential in planta using hydrogel nanoreporters, *Proc. Natl. Acad. Sci. U. S. A.*, 2021, **118**, e2008276118.
30 S. Han, W. Kim, H. J. Lee, R. Joyce and J. Lee, Continuous and Real-Time Measurement of Plant Water Potential Using an AAO-Based Capacitive Humidity Sensor for Irrigation Control, *ACS Appl. Electron. Mater.*, 2022, **4**, 5922–5932.
31 P. Jain, *et al.*, Localized measurements of water potential reveal large loss of conductance in living tissues of maize leaves, *Plant Physiol.*, 2024, **194**, 2288–2300.
32 W. Shi, *et al.*, Passive water ascent in a tall, scalable synthetic tree, *Sci. Rep.*, 2020, **10**, 230.
33 S. Poudel, A. Zou and S. C. Maroo, Disjoining pressure driven transpiration of water in a simulated tree, *J. Colloid Interface Sci.*, 2022, **616**, 895–902.
34 M. T. Tyree, The Cohesion-Tension theory of sap ascent: current controversies, *J. Exp. Bot.*, 1997, **48**(315), 1753–1765.
35 U. Zimmermann, H. Schneider, L. H. Wegner and A. Haase, Water ascent in tall trees: does evolution of land plants rely on a highly metastable state?, *New Phytol.*, 2004, **162**, 575–615.
36 I.-T. Chen, *et al.*, Stability Limit of Water by Metastable Vapor–Liquid Equilibrium with Nanoporous Silicon Membranes, *J. Phys. Chem. B*, 2016, **120**, 5209–5222.
37 G. W. Koch, S. C. Sillett, G. M. Jennings and S. D. Davis, The limits to tree height, *Nature*, 2004, **428**, 851–854.
38 P. Van Carey, *Liquid–Vapor Phase-Change Phenomena*, CRC Press, Boca Raton, 2020.
39 J. Yin, *et al.*, Generating electricity by moving a droplet of ionic liquid along graphene, *Nat. Nanotechnol.*, 2014, **9**, 378–383.
40 J. Yin, *et al.*, Waving potential in graphene, *Nat. Commun.*, 2014, **5**, 3582.
41 A. T. Liu, *et al.*, Electrical Energy Generation via Reversible Chemical Doping on Carbon Nanotube Fibers, *Adv. Mater.*, 2016, **28**, 9752–9757.
42 Y. Kunai, *et al.*, Observation of the Marcus Inverted Region of Electron Transfer from Asymmetric Chemical Doping of Pristine (*n*, *m*) Single-Walled Carbon Nanotubes, *J. Am. Chem. Soc.*, 2017, **139**, 15328–15336.
43 A. T. Liu, *et al.*, Direct Electricity Generation Mediated by Molecular Interactions with Low Dimensional Carbon Materials—A Mechanistic Perspective, *Adv. Energy Mater.*, 2018, **8**, 1802212.
44 O. Stern, ZUR THEORIE DER ELEKTROLYTISCHEN DOPPELSCHICHT, *Z. Für Elektrochem. Angew. Phys. Chem.*, 1924, **30**, 508–516.
45 G. Quincke, Ueber die Fortführung materieller Theilchen durch strömende Elektricität, *Ann. Phys.*, 1861, **189**, 513–598.
46 S. Wall, The history of electrokinetic phenomena, *Curr. Opin. Colloid Interface Sci.*, 2010, **15**, 119–124.
47 F. H. J. Van Der Heyden, D. Stein and C. Dekker, Streaming Currents in a Single Nanofluidic Channel, *Phys. Rev. Lett.*, 2005, **95**, 116104.
48 M. Mooney, Electrophoresis and the Diffuse Ionic Layer, *J. Phys. Chem.*, 1931, **35**, 331–344.
49 S. Chaurasia, R. Kumar, T. Tabrizizadeh, G. Liu and K. Stamplecoskie, All-Weather-Compatible Hydrovoltaic Cells Based on Al_2O_3 TLC Plates, *ACS Omega*, 2022, **7**, 2618–2623.
50 J. Bae, T. G. Yun, B. L. Suh, J. Kim and I.-D. Kim, Self-operating transpiration-driven electrokinetic power generator with an artificial hydrological cycle, *Energy Environ. Sci.*, 2020, **13**, 527–534.
51 S. G. Yoon, *et al.*, Evaporative electrical energy generation via diffusion-driven ion-electron-coupled transport in semiconducting nanoporous channel, *Nano Energy*, 2021, **80**, 105522.
52 R. Cazzolla Gatti, *et al.*, The number of tree species on Earth, *Proc. Natl. Acad. Sci. U. S. A.*, 2022, **119**, e2115329119.
53 E. Nabeshima, T. Kubo and T. Hiura, Variation in tree diameter growth in response to the weather conditions and tree size in deciduous broad-leaved trees, *For. Ecol. Manage.*, 2010, **259**, 1055–1066.
54 R. Liang, Y. Sun, S. Qiu, B. Wang and Y. Xie, Relative effects of climate, stand environment and tree characteristics on annual tree growth in subtropical Cunninghamia lanceolata forests, *Agric. For. Meteorol.*, 2023, **342**, 109711.
55 L. Fernández-de-Uña, J. Martínez-Vilalta, R. Poyatos, M. Mencuccini and N. G. McDowell, The role of height-driven constraints and compensations on tree vulnerability to drought, *New Phytol.*, 2023, **239**, 2083–2098.
56 D. Whitehead, W. R. N. Edwards and P. G. Jarvis, Conducting sapwood area, foliage area, and permeability in mature trees of Piceasitchensis and Pinuscontorta, *Can. J. For. Res.*, 1984, 940–947, DOI: 10.1139/x84-166.
57 L. Fernández-de-Uña, J. Martínez-Vilalta, R. Poyatos, M. Mencuccini and N. G. McDowell, The role of height-driven constraints and compensations on tree vulnerability to drought, *New Phytol.*, 2023, **239**, 2083–2098.
58 F. C. Meinzer, B. Lachenbruch and T. E. Dawson, *Size- and Age-Related Changes in Tree Structure and Function*, Springer Netherlands, Dordrecht, 2011, vol. 4.
59 A. R. Ambrose, *et al.*, Effects of height on treetop transpiration and stomatal conductance in coast redwood (Sequoia sempervirens), *Tree Physiol.*, 2010, **30**, 1260–1272.
60 J. A. Rosell, S. Gleason, R. Méndez-Alonzo, Y. Chang and M. Westoby, Bark functional ecology: evidence for tradeoffs, functional coordination, and environment producing bark diversity, *New Phytol.*, 2014, **201**, 486–497.
61 S. J. Tumber-Dávila, H. J. Schenk, E. Du and R. B. Jackson, Plant sizes and shapes above and belowground and their interactions with climate, *New Phytol.*, 2022, **235**, 1032–1056.
62 Y. Fan, G. Miguez-Macho, E. G. Jobbágy, R. B. Jackson and C. Otero-Casal, Hydrologic regulation of plant rooting depth, *Proc. Natl. Acad. Sci. U. S. A.*, 2017, **114**, 10572–10577.
63 A. Tariq, *et al.*, Plant root mechanisms and their effects on carbon and nutrient accumulation in desert ecosystems

under changes in land use and climate, *New Phytol.*, 2024, **242**, 916–934.
64 X. Li, *et al.*, Ion-selective vermiculite nanochannel membrane with water anchoring effect for efficient energy recovery from water evaporation, *J. Membr. Sci.*, 2025, **718**, 123698.
65 J. Chi, *et al.*, Harvesting Water-Evaporation-Induced Electricity Based on Liquid–Solid Triboelectric Nanogenerator, *Adv. Sci.*, 2022, **9**, 2201586.
66 S. Jiao, *et al.*, Evaporation Driven Hydrovoltaic Generator Based on Nano-Alumina-Coated Polyethylene Terephthalate Film, *Polymers*, 2023, **15**, 4079.
67 L. Li, *et al.*, A novel, flexible dual-mode power generator adapted for wide dynamic range of the aqueous salinity, *Nano Energy*, 2021, **85**, 105970.
68 L. Li, *et al.*, Sustainable and flexible hydrovoltaic power generator for wearable sensing electronics, *Nano Energy*, 2020, **72**, 104663.
69 X. Shi, *et al.*, A Kirigami-Driven Stretchable Paper-Based Hydrovoltaic Electricity Generator, *Adv. Funct. Mater.*, 2025, 2419753, DOI: 10.1002/adfm.202419753.
70 X. Wang, *et al.*, Composite laminar membranes for electricity generation from water evaporation, *Nano Res.*, 2024, **17**, 307–311.
71 C. Shao, *et al.*, Large-Scale Production of Flexible, High-Voltage Hydroelectric Films Based on Solid Oxides, *ACS Appl. Mater. Interfaces*, 2019, **11**, 30927–30935.
72 J. Eun and S. Jeon, Janus Membrane-Based Hydrovoltaic Power Generation with Enhanced Performance under Suppressed Evaporation Conditions, *ACS Appl. Mater. Interfaces*, 2023, **15**, 50126–50133.
73 T. Tabrizizadeh, *et al.*, Water-Evaporation-Induced Electric Generator Built from Carbonized Electrospun Polyacrylonitrile Nanofiber Mats, *ACS Appl. Mater. Interfaces*, 2021, **13**, 50900–50910.
74 Y. Wang, *et al.*, 3D dendritic hierarchically gradient nanoflowers *in situ* grown on conductive substrates for efficient hydrovoltaic power generation, *Energy Environ. Sci.*, 2024, **17**, 4780–4793.
75 M. Cao, *et al.*, Ambient-Dried Nanocellulose Composite Aerogels for Enhanced Hydrovoltaic Electricity Generation, *Adv. Funct. Mater.*, 2024, 2418823, DOI: 10.1002/adfm.202418823.
76 J. H. Park, S. H. Park, J. Lee and S. J. Lee, Solar Evaporation-Based Energy Harvesting Using a Leaf-Inspired Energy-Harvesting Foam, *ACS Sustainable Chem. Eng.*, 2021, **9**, 5027–5037.
77 S. Yang, *et al.*, Ionic Hydrogel for Efficient and Scalable Moisture-Electric Generation, *Adv. Mater.*, 2022, **34**, 2200693.
78 W. Yuan, *et al.*, Scalable MXene/Sepiolite film-based hydrovoltaic generators with outstanding output power, *Chem. Eng. J.*, 2024, **499**, 155952.
79 A. Lintunen and T. Kalliokoski, The effect of tree architecture on conduit diameter and frequency from small distal roots to branch tips in Betula pendula, Picea abies and Pinus sylvestris, *Tree Physiol.*, 2010, **30**, 1433–1447.
80 S. Lv, *et al.*, Xylem anatomy differentiation explains coordinated variation of economic and hydraulic traits in urban tree species, *BMC Plant Biol.*, 2025, **25**, 1549.
81 P. J. Hudson, J. Razanatsoa and T. S. Feild, Early vessel evolution and the diverisification of wood function: Insights from Malagasy Canellales, *Am. J. Bot.*, 2010, **97**, 80–93.
82 U. G. Hacke, J. S. Sperry and J. Pittermann, Efficiency *Versus* Safety Tradeoffs for Water Conduction in Angiosperm Vessels *Versus* Gymnosperm Tracheids, *Vascular Transport in Plants*, Elsevier, 2005, pp. 333–353, DOI: 10.1016/B978-012088457-5/50018-6.
83 M. Zhang, *et al.*, Comparison of wood physical and mechanical traits between major gymnosperm and angiosperm tree species in China, *Wood Sci. Technol.*, 2017, **51**, 1405–1419.
84 C. B. Williams, *et al.*, Axial variation of xylem conduits in the Earth's tallest trees, *Trees*, 2019, **33**, 1299–1311.
85 S. Jansen, P. Baas, P. Gasson, F. Lens and E. Smets, Variation in xylem structure from tropics to tundra: Evidence from vestured pits, *Proc. Natl. Acad. Sci. U. S. A.*, 2004, **101**, 8833–8837.
86 X. Zhou, *et al.*, Harvesting Electricity from Water Evaporation through Microchannels of Natural Wood, *ACS Appl. Mater. Interfaces*, 2020, **12**, 11232–11239.
87 T. Anwar and G. Tagliabue, Salinity-dependent interfacial phenomena toward hydrovoltaic device optimization, *Device*, 2024, **2**, 100287.
88 J. Garemark, *et al.*, Advancing Hydrovoltaic Energy Harvesting from Wood through Cell Wall Nanoengineering, *Adv. Funct. Mater.*, 2023, **33**, 2208933.
89 B. Shao, *et al.*, Bioinspired Hierarchical Nanofabric Electrode for Silicon Hydrovoltaic Device with Record Power Output, *ACS Nano*, 2021, **15**, 7472–7481.
90 S. Yu, *et al.*, Interlayer mediated water motion-induced ionovoltaic electricity generation, *Nano Energy*, 2024, **123**, 109345.
91 Z. Liu, *et al.*, Tortuosity regulation of two-dimensional nanofluidic films for water evaporation-induced electricity generation, *Nano Res.*, 2024, **17**, 6192–6202.
92 M. Wu, *et al.*, Printed Honeycomb-Structured Reduced Graphene Oxide Film for Efficient and Continuous Evaporation-Driven Electricity Generation from Salt Solution, *ACS Appl. Mater. Interfaces*, 2021, **13**, 26989–26997.
93 M. Wu, *et al.*, High evaporation rate and electrical conductivity synergistically boosting porous rGO/CNT Film for water evaporation-driven electricity generation, *Nano Energy*, 2023, **116**, 108771.
94 T. Ding, *et al.*, All-Printed Porous Carbon Film for Electricity Generation from Evaporation-Driven Water Flow, *Adv. Funct. Mater.*, 2017, **27**, 1700551.
95 B. Ji, *et al.*, Intelligent multiple-liquid evaporation power generation platform using distinctive Jaboticaba-like carbon nanosphere@TiO_2 nanowires, *J. Mater. Chem. A*, 2019, **7**, 6766–6772.
96 S.-H. Lee, *et al.*, Cost-effective moisture-induced electrical power generators for sustainable electrodialysis desalination, *Nano Energy*, 2024, **126**, 109683.
97 S.-H. Lee, *et al.*, A novel water electrolysis hydrogen production system powered by a renewable hydrovoltaic power generator, *Chem. Eng. J.*, 2024, **495**, 153411.

98 S.-H. Lee, *et al.*, Water-Based Generators with Cellulose Acetate: Uncovering the Mechanisms of Power Generation, *Polymers*, 2024, **16**, 433.
99 J. Li, *et al.*, Surface functional modification boosts the output of an evaporation-driven water flow nanogenerator, *Nano Energy*, 2019, **58**, 797–802.
100 J. Li, Y. Dai, S. Jiao and X. Liu, MOFs/Ketjen Black-Coated Filter Paper for Spontaneous Electricity Generation from Water Evaporation, *Polymers*, 2022, **14**, 3509.
101 L. Li, *et al.*, Ionovoltaic natural evaporation-induced electrical energy harvesting for green hydrogen generation, *Nano Energy*, 2025, **136**, 110731.
102 L. Li, *et al.*, A Flexible Tough Hydrovoltaic Coating for Wearable Sensing Electronics, *Adv. Mater.*, 2023, **35**, 2304099.
103 N. Hossain, *et al.*, Hydrovoltaic energy harvesting from nut shells, *Energy Environ. Mater.*, 2025, **8**, e70017.
104 Y. Liu, *et al.*, A fabric-based hydrovoltaic electricity generator with multi-component carbon black for sustainable energy output, *RSC Adv.*, 2024, **14**, 18832–18837.
105 Z. Liu, *et al.*, Self-floating Janus hydrovoltaics for sustainable electricity generation, *J. Power Sources*, 2025, **628**, 235934.
106 B. Tian, *et al.*, Integrating reduced graphene oxides and PPy nanoparticles for enhanced electricity from water evaporation, *Int. J. Smart Nano Mater.*, 2023, **14**, 230–242.
107 Y. Wang, *et al.*, Graphene oxide and carbon black synergistic coated cotton fabric for enhancing energy harvesting from water droplets, *Carbon*, 2024, **223**, 119008.
108 R. Yuan, *et al.*, Hermetic hydrovoltaic cell sustained by internal water circulation, *Nat. Commun.*, 2024, **15**, 9796.
109 T. G. Yun, *et al.*, Ion-permselective conducting polymer-based electrokinetic generators with maximized utility of green water, *Nano Energy*, 2022, **94**, 106946.
110 G. Zhang, *et al.*, Harvesting environment energy from water-evaporation over free-standing graphene oxide sponges, *Carbon*, 2019, **148**, 1–8.
111 X. Zhang, *et al.*, Fabrication and study of a high output power flexible fabric hydrovoltaic generator, *J. Mater. Chem. A*, 2023, **11**, 26173–26182.
112 G. Luo, *et al.*, Highly Stretchable, Knittable, Wearable Fiberform Hydrovoltaic Generators Driven by Water Transpiration for Portable Self-Power Supply and Self-Powered Strain Sensor, *Small*, 2024, **20**, 2306318.
113 M. Anys and M. Weiler, Controls on Tree Transpiration Dynamics in an Urban Environment, *Agric. For. Meteorol.*, 2024, **372**, 110726.
114 C. Bachofen, *et al.*, Tree water uptake patterns across the globe, *New Phytol.*, 2024, **242**, 1891–1910.
115 Q. Hu, *et al.*, Hydrovoltaic electricity generation induced by living leaf transpiration, *Nat. Water*, 2024, **2**, 988–998.
116 Q. Hu, *et al.*, Hydrovoltaic electricity generation induced by living leaf transpiration, *Nat. Water*, 2024, **2**, 988–998.
117 Z. Li, *et al.*, Polyaniline-Coated MOFs Nanorod Arrays for Efficient Evaporation-Driven Electricity Generation and Solar Steam Desalination, *Adv. Sci.*, 2021, **8**, 2004552.
118 X. Piao, *et al.*, Water-evaporation induced electricity generation inspired by natural tree transpiration, *Sustainable Mater. Technol.*, 2024, **39**, e00836.
119 J. Zhang, *et al.*, Paper-Based Hydroelectric Generators for Water Evaporation-Induced Electricity Generation, *Adv. Sci.*, 2023, **10**, 2304482.
120 S. Sudhir, A. Arunprasath and V. Sankara Vel, A critical review on adaptations, and biological activities of the mangroves, *J. Nat. Pestic. Res.*, 2022, **1**, 100006.
121 A. K. Parida and A. B. Das, Salt tolerance and salinity effects on plants: a review, *Ecotoxicol. Environ. Saf.*, 2005, **60**, 324–349.
122 S. Naseer, *et al.*, Casparian strip diffusion barrier in *Arabidopsis* is made of a lignin polymer without suberin, *Proc. Natl. Acad. Sci. U. S. A.*, 2012, **109**, 10101–10106.
123 Y. Liu, *et al.*, A fabric-based hydrovoltaic electricity generator with multi-component carbon black for sustainable energy output, *RSC Adv.*, 2024, **14**, 18832–18837.
124 R. Kumar, T. Tabrizizadeh, S. Chaurasia, G. Liu and K. Stamplecoskie, Hydrovoltaic power generation from multiwalled carbon nanotubes, *Sustainable Energy Fuels*, 2022, **6**, 1141–1147.
125 W. Yuan, *et al.*, Scalable MXene/Sepiolite film-based hydrovoltaic generators with outstanding output power, *Chem. Eng. J.*, 2024, **499**, 155952.
126 J. Bae, *et al.*, Towards Watt-scale hydroelectric energy harvesting by $Ti_3C_2T_x$-based transpiration-driven electrokinetic power generators, *Energy Environ. Sci.*, 2022, **15**, 123–135.
127 G. C. Beaton, R. Kumar, N. Neokleous, G. Liu and K. Stamplecoskie, Gold nanoparticle decorated filter papers as hydrovoltaic devices, *Sustainable Energy Fuels*, 2022, **6**, 4645–4651.
128 Z. Zhou, *et al.*, Self-powered TpPa/PAN membrane-based flexible hydrovoltaic sensor for real-time Congo red monitoring, *Sens. Actuators, B*, 2025, **432**, 137507.
129 H. Ding, *et al.*, Hydrovoltaic Effect Coupling with Capacitor Amplification: A Mode for Sensitive Self-Powered Electrochemical Sensing, *Anal. Chem.*, 2023, **95**, 12595–12599.
130 Y. Lin, *et al.*, Evaporation-Driven Fabric for Synergistic Water-Electricity-Lithium Co-Production, *Adv. Mater.*, 2025, **37**, e06956.
131 X. Chen, *et al.*, Spatially separated crystallization for selective lithium extraction from saline water, *Nat. Water*, 2023, **1**, 808–817.
132 C. Liu, *et al.*, Lithium Extraction from Seawater through Pulsed Electrochemical Intercalation, *Joule*, 2020, **4**, 1459–1469.
133 Q. Liu, *et al.*, Fully Printable Manufacturing of Miniaturized, Highly Integrated, Flexible Evaporation-Driven Electricity Generator Arrays, *Adv. Sci.*, 2025, **12**, 2413779.
134 L. Wang, W. Zhang and Y. Deng, High-voltage hydrovoltaic generator based on micro/nano multi-scale superhydrophilic SiO_2 @activated carbon with enhanced capillary infiltration performance, *Mater. Horiz.*, 2025, **12**, 8724–8733.
135 W. Gao, *et al.*, Fully integrated wearable sensor arrays for multiplexed in situ perspiration analysis, *Nature*, 2016, **529**, 509–514.